Rijksuniversiteit Groningen

Bachelor Thesis

In the Shape of Emptiness

Dark Energy and the Evolution of Voids in the Homogeneous Ellipsoidal Model

Author:
Giada Selva

Supervisor:
Rien van de Weijgaert

Contents

1 Abstract

In this thesis, a numerical solver was developed for the homogeneous ellipsoidal model, capable of evolving arbitrary initial conditions for isolated voids or overdensities. The solver tracks the time evolution of the principal axes of ellipsoidal regions, allowing for a detailed study of their shape dynamics over cosmic time.

The model isolates and quantifies the contributions of three fundamental physical forces: self-gravity, the tidal fields, and dark energy contribution. A striking result of this analysis is the clear separation of their roles: dark energy, when acting alone, contributes only to isotropic expansion, uniformly expanding the void without altering its shape. In contrast, the tidal field causes the anisotropy, deforming the void as it evolves.

In the final part of the study, model predictions are compared against data extracted from the TNG50 cosmological simulation. This comparison serves as a test of the model's validity and highlights both its strengths and limitations when applied to realistic cosmic environments. The results demonstrate that the model reproduces key trends observed in the simulation, particularly the emergence of anisotropy in void evolution, while also suggesting directions for future refinement and extension.

2 Motivation and Scope of the Thesis

This thesis investigates the evolution of cosmic voids through the homogeneous ellipsoidal model. This model was originally developed by (Lin et al., 1965; Bond & Myers, 1996) to study the collapse of overdense regions in the early Universe . Despite its relevance, one of the main assumptions built into its framework is the internal homogeneity, which naturally represents a significant limitation when modeling non-linear overdensities. Voids, on the other hand, can provide an arguably much more suitable environment for such an approximation, since their density profiles evolve smoothly (Icke, 1984; Desjacques, 2008).

In order to test the homogeneous ellipsoidal model in the context of cosmic voids, this research investigates the evolution of a idealized singular underdensity, only influenced by the effect of 3 forces: internal self gravitation, anisotropic tidal fields and the dark energy contribution.

The understanding and testing of the latter, is in particular, one of the goals of this thesis. The main interrogative is if dark energy influences voids merely through homogeneous expansion, or if it plays a role in the shape evolution, e.g., by affecting expansion rates along the different axes or changing the timing of the most main evolutionary stages. In the second part of this work, I was interested in testing the physical reliability of the model. To do so, the data obtained from the homogeneous ellipsoidal model has been compared to more realistic underdense regions in the IllustrisTNG-Dark simulation. This step is intended to check if the ellipsoidal approximation reproduces realistic voids' large-scale morphology and evolution and hence the usefulness of the model in ΛCDM cosmology.

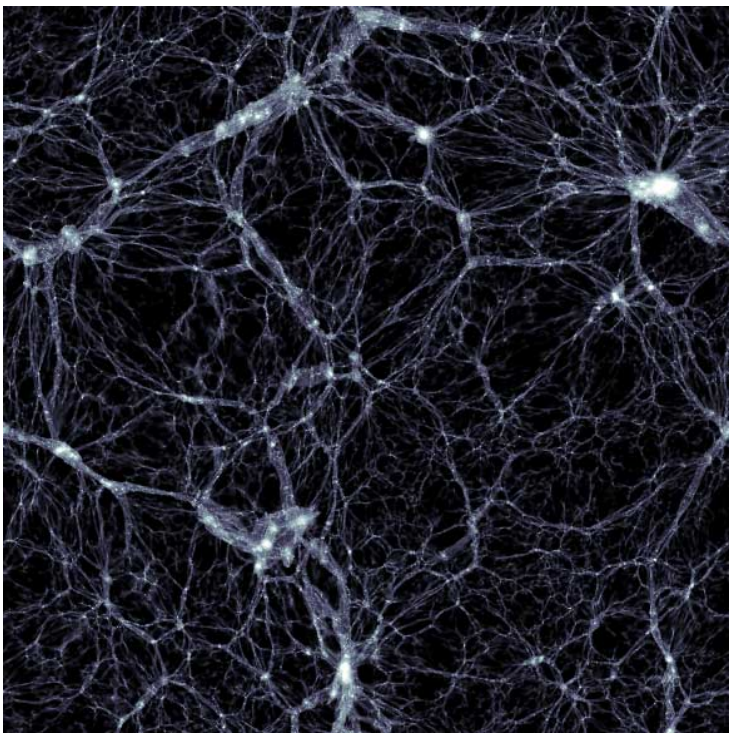

Figure 1: **Dark Matter Distribution at $z = 0$ in the Illustris Simulation.** The dark matter density field is shown in a thin slice (thickness $\sim 104\,\mathrm{kpc}$), revealing the large-scale cosmic web structure. Filaments, nodes, and expansive voids are visible, with underdense regions appearing as dark spaces between denser structures. Adapted from Haider et al. (2016).

3 The Primordial Design: How the Cosmic Web Took Shape

Throughout most of the twentieth century, the Universe was thought to be highly homogeneous and isotropic on the very largest scales. The distribution of galaxies was believed to be random with only a few small groups and superclusters. The formation of cosmic structure was described using simplified models of spherical collapse, which found their origin in tiny perturbations in an otherwise homogeneous density field. There was little observational or theoretical motivation to expect any coherent geometry across tens or hundreds of Mpc.

This perspective started to change with the emergence of modern cosmological theories involving cold dark matter and gravitational instability. Although the main assumptions of uniformity were still applied, early models have already suggested that a large-scale structure could arise from local gravitational effects. Crucial progress was made possible by the work of (Zel'dovich, 1970), in which he formulated an anisotropic collapse model where matter initially contracts along one axis to form walls, then along a second to form filaments, and ultimately collapses into compact clusters. This concept was formalized in the Zel'dovich approximation and a foundation of structure formation theory. It revealed the evolution of the Universe not as a group of disconnected clumps, but as a connected series of sheet-like, filamentary, and nodal structures.

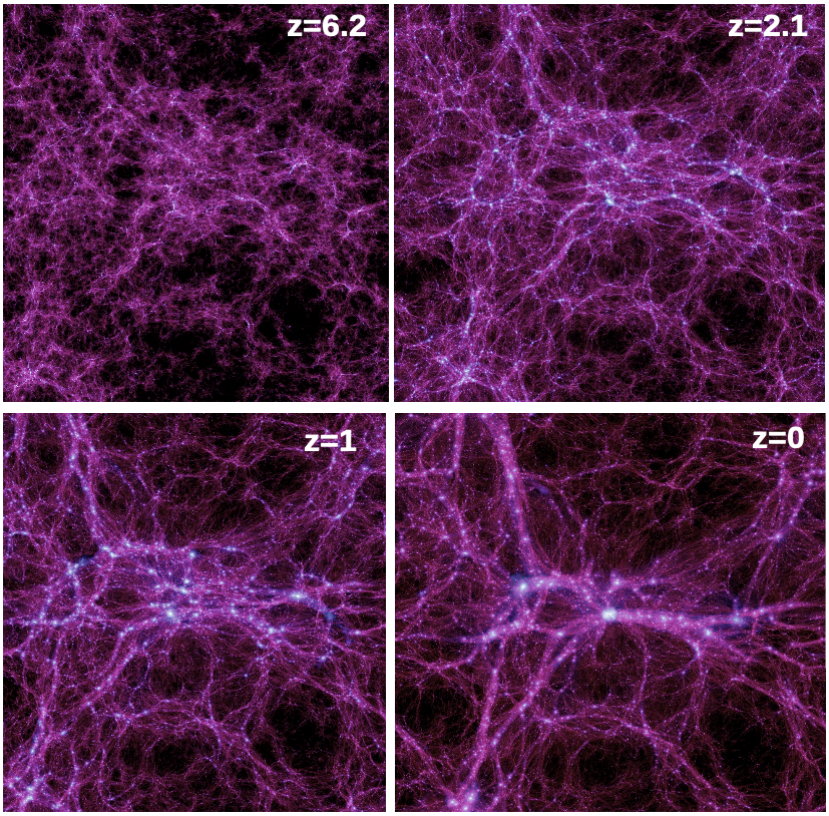

Figure 2: **Growth of cosmic structure over time** Projected dark matter density from the Millennium-II simulation at redshifts $z = 6.2$, 2.1, 1, and 0. The initially smooth density field evolves the cosmic web. Adapted from Boylan-Kolchin et al. (2009) via Zavala & Frenk (2021).

Alongside, the concept of cold dark matter being involved in structure formation gained popularity, particularly after the work of (Blumenthal et al., 1984). This study described a model in which small-scale substructure in the dark matter distribution triggered the formation

of galaxies. These results were supported by simulations that quickly became very reliable. For instance, (Springel et al., 2006), demonstrated when viewed at higher resolution,that the seemingly smooth density field was, in fact, composed of complex structures.

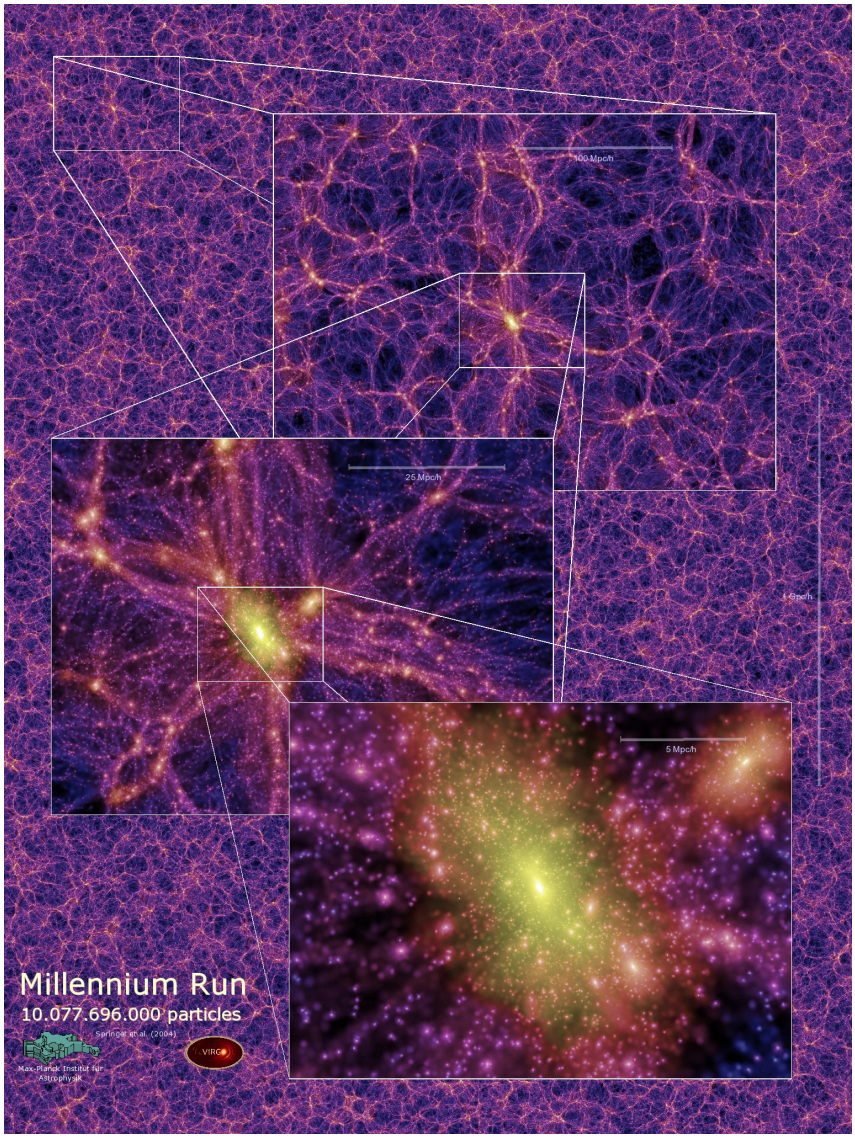

Figure 3: **Hierarchical Structure in the Millennium Simulation.** Zoom-ins reveal the nested dark matter substructure across cosmic scales. Adapted from Springel et al. (2005).

During the same time, two main points of view on large-scale structure started to develop. The "Western" view was based on hierarchical clustering (Peebles, 1980) and it explained structure in a bottom-up fashion: from small scales upward. Whereas, the "Russian" perspective stressed large-scale coherence due to the statistical character of the initial density field. (Bond et al., 1996) was able to reconcile both within a single paradigm by formalizing the concept of the cosmic web. Employing the power spectrum of the Gaussian random field (Bardeen et al., 1986), they demonstrated that the tidal field and initial density already contained within them the geometry that would be revealed later through nonlinear evolution. Their simulation indicated that voids, filaments, walls, and clusters were not fleeting emergents, but enhanced manifestations of early universe fluctuations.

This process was further investigated by (Doroshkevich, 1970), who demonstrated that the eigenvalues of the primordial tidal tensor predicted anisotropic collapse along privileged axes. Matter would flow from underdense voids into walls, from walls into filaments, and then from filaments into overdense nodes. (Libeskind et al., 2018) and (Feldbrugge & Van De Weygaert, 2023) developed this concept further, highlighting how gravitational instability amplifies the contrast of the field, so that dense regions grow denser, while voids empty out. This process of self-enforcing was compared with the "Matthew effect" by (Ryden, 2003), which is named after the passage in the Bible where the rich get richer, and the poor lose even the little that they possess.

Computationally, these predictions have been tested through N-body and confirmed with redshift surveys of galaxies. (Springel et al., 2006) and (Cautun et al., 2014) illustrated the hierarchical build-up of the web, revealing how mass streams along this network and accumulates structure over time. Voids, which occupy most of the cosmic web's volume, play an important active role in this evolution. They grow as matter streams towards walls and filaments, sculpting the web's foam-like topology (van de Weygaert & Schaap, 2009).

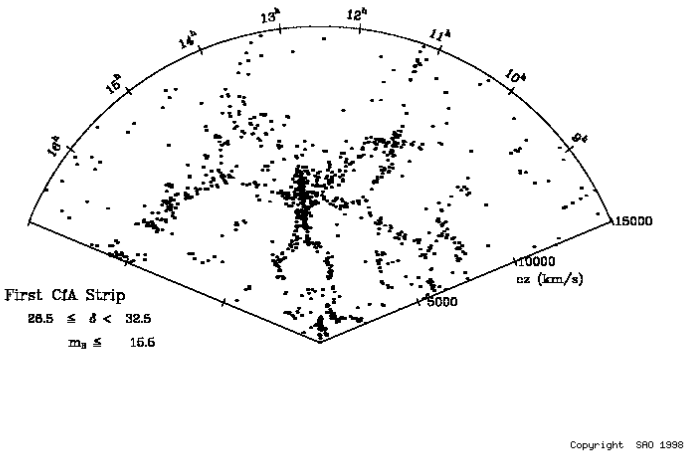

Figure 4: **The CfA Redshift Survey** revealed the first observational evidence of large-scale filamentary structure.

As simulations became more sophisticated, so did our capacity for observation. The CfA Redshift Survey first gave visual proof of large-scale structure, with filamentary clustering and enormous voids (de Lapparent et al., 1986). The 2dF Galaxy Redshift Survey and the Sloan Digital Sky Survey (SDSS) (York et al., 2000) then mapped millions of galaxies and verified the complex connectivity envisioned decades before. Observational features such as "fingers of God" and "stickman" distortions further emphasized the dynamical richness of the cosmic web and the effect of peculiar velocities in denser regions (Peacock et al., 2001; Ryden & Melott, 1996).

4 Dark Energy and the Accelerating Universe

The concept of dark energy reentered modern cosmology at the turn of the 21st century,yet it has its roots in the very early days of general relativity. Einstein first introduced a cosmological constant, Λ, when he was deriving the field equations in order to guarantee a static universe. This was not mathematically necessary but rather a reaction to the bias then that the Universe was static. After Hubble observed the expansion of the universe, Λ was no longer needed and thus was omitted.

The cosmological constant returned after it was realized that the expansion of the Universe is accelerating. Observations of type Ia supernovae revealed that distant supernovae were dimmer than expected, which implied they were more distant than expected in a decelerating model (Riess, 1998; Perlmutter, 1999). The finding indicates the presence of a repulsive element in the Universe's energy budget.

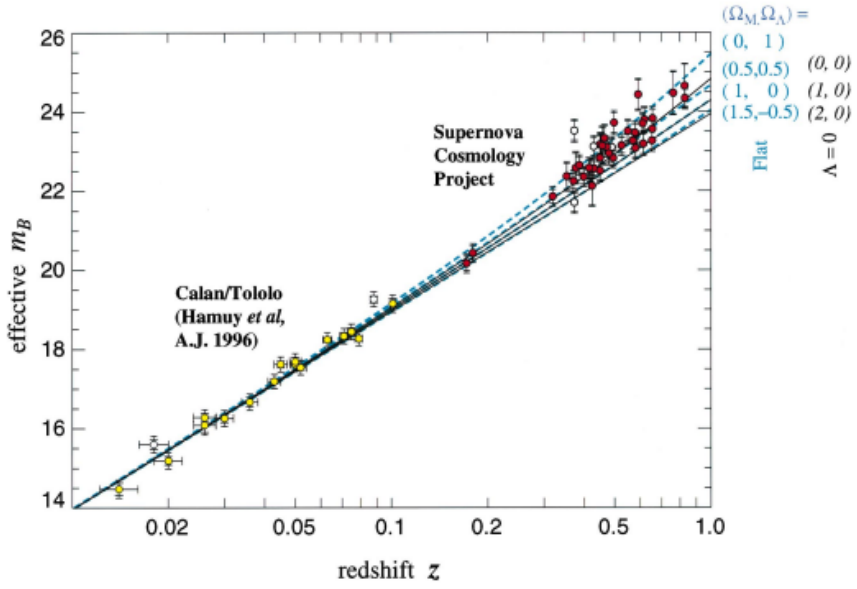

Figure 5: **Hubble Diagram of Type Ia Supernovae.** Data from the Calán/Tololo Survey and the Supernova Cosmology Project (Perlmutter, 1999). The supernovae appear dimmer than expected in a decelerating universe, implying accelerated cosmic expansion and the presence of dark energy.

This component, now known as dark energy, accounts for approximately 68% of the total energy density (Frieman et al., 2008; Mortonson et al., 2014). Dark energy is modeled as a fluid with negative pressure in the standard ΛCDM model, whose equation-of-state parameter $w = p/\rho$ and satisfies $w < -1/3$. The simplest example is a constant energy density with $w = -1$, consistent with a cosmological constant.

Measurements from supernovae, baryon acoustic oscillations (BAO), and the cosmic microwave background (CMB) constrain the value of w to be close to -1 (Kowalski et al., 2008; Hicken et al., 2009; Amanullah et al., 2010). The dark energy is still a mystery, however. Some models permit w to change in time or even go below -1, so-called phantom regime (Linder, 2008; Caldwell, 2009). In these models, the density of dark energy grows over time, resulting in a future in which the expansion continues to accelerate indefinitely. If this acceleration becomes sufficiently energetic, gravitationally bound objects would be ripped apart, ending in a

speculative event known as the "Big Rip."

The dark energy behavior controls the ultimate fate of the Universe in the long term. A constant Λ leads to eternal acceleration, but time-dependent models allow for eventual deceleration, recollapse, or catastrophic expansion. In each case, there are analogous behaviors for $w(z)$, the equation-of-state function as a function of redshift.

In spite of the fact that its gravitational impact is well established, dark energy does not have any confirmed non-gravitational interaction, unlike dark matter. Dark energy is not clumped gravitationally, in contrast to matter, and does not generate local signatures such as lensing peaks or small-scale clustering power. Its presence reveals itself within the large-scale geometry and expansion history.

Nowadays astronomers aim to quantify the precision of the expansion history $H(z)$ and growth of structure $f(z)\sigma_8(z)$ with increasing accuracy. Upcoming surveys like DESI, Euclid, and the Vera Rubin Observatory will further constrain w and any potential evolution.

Table 1: **Cosmic density parameters** at the current time, including 68% confidence limits, (Bos, 2016)(Planck Collaboration et al., 2016)

component	symbol	value
baryonic matter	Ω_b	0.0484 ± 0.0005
dark matter	Ω_d	0.256 ± 0.004
radiation	Ω_r	0.000092 ± 0.000004
dark energy	Ω_Λ	0.692 ± 0.012

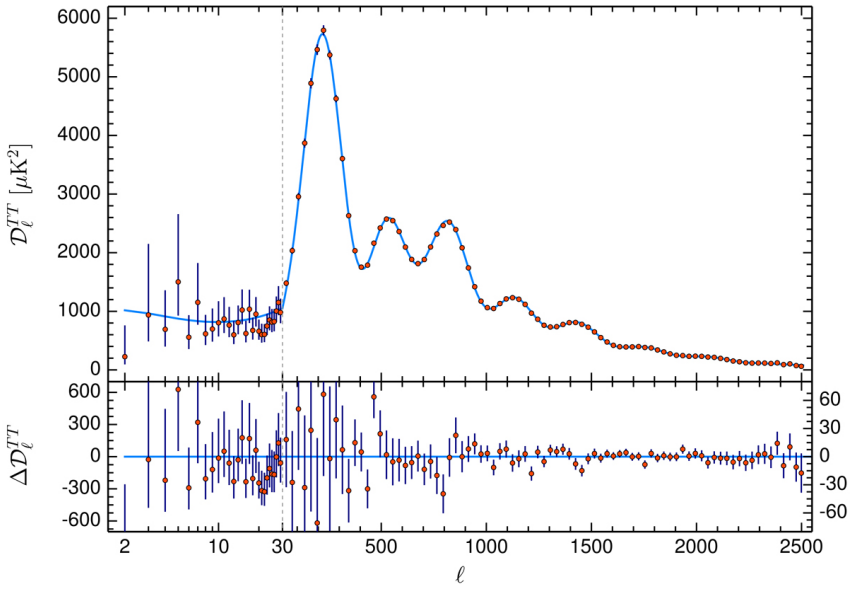

Figure 6: **CMB Temperature Power Spectrum from *Planck*.** The power spectrum D_ℓ^{TT} shows acoustic peaks representing important cosmological information. The position and height of the first peak, along with subsequent features, constrain the total energy density and support a dark energy–dominated Universe. Lower panel: residuals from the best-fit ΛCDM model (Planck Collaboration et al., 2020).

5 Cosmic Voids: From Emptiness to Structure

When we think of a "void," we imagine emptiness: simply nothing. Yet in cosmology, voids anything but insignificant. Cosmic voids are large regions, characterized by being underdense with respect to the background, typically sized between 10 and 50 h^{-1}Mpc

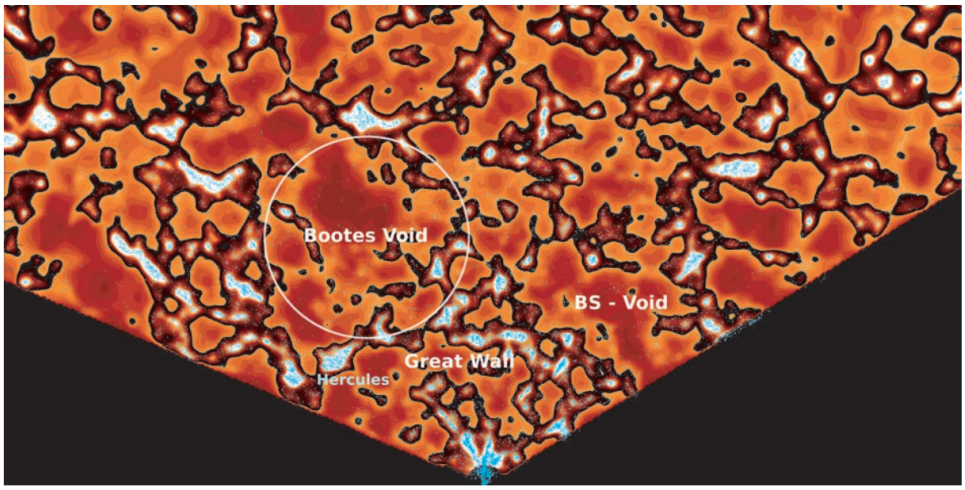

Figure 7: **Cosmic web in SDSS.** DTFE density map from SDSS showing a 12 h^{-1}Mpc slice. Underdense regions (red) reveal large voids like the Boötes and BS voids. Overdensities (bright) trace the Great Wall and Hercules supercluster. From van de Weygaert & Platen (2011a).

Voids were first identified as physical structures in galaxy redshift surveys in the 1970s and 1980s (Chincarini & Rood, 1975; Gregory & Thompson, 1978; Einasto et al., 1980; Kirshner et al., 1981). The discovery of the Boötes void (Kirshner et al., 1981), and the CfA redshift slice (de Lapparent et al., 1986) revealed galaxies distributed in filaments, walls, and clusters with enormous, apparently empty regions between them. These voids were emphasized even more in subsequent surveys such as the 2dFGRS and SDSS (Colless et al., 2003; Tegmark et al., 2004; Huchra et al., 2012). Even more recently, voids have been traced in deep surveys such as VIPERS (Guzzo et al., 2014), and even reconstructed dark matter maps (Kitaura et al., 2012; Leclercq, 2015), demonstrating that voids are not observation artifacts but an actual component of structure formation.

Theoretical and numerical studies confirm that voids are natural outcomes of gravitational evolution in a Universe with initial Gaussian fluctuations (Icke, 1984; Dubinski et al., 1993; Sheth & van de Weygaert, 2004). In the linear regime, underdense regions expand faster than the background, their density contrast δ becoming increasingly negative. This leads to the evacuation of matter and the development of a flat, low-density interior with a steep edge: a "bucket-shaped" profile (van de Weygaert & van Kampen, 1993; Platen et al., 2008). This expansion proceeds in near isolation until interactions with surrounding structures start to influence their shape.

While early models assumed spherical symmetry, real voids are neither spherical nor isolated. They are strongly shaped by the large-scale tidal field. Voids tend to elongate in directions set by the surrounding matter distribution (Bond et al., 1996), and simulations confirm that their shape evolution correlates with the local tidal tensor (Platen et al., 2008). This makes voids excellent probes of cosmic environment, and sensitive to both dark energy and gravitational physics (Lee & Park, 2009; Bos et al., 2012).

Voids also evolve hierarchically. Small voids embedded within larger underdensities merge

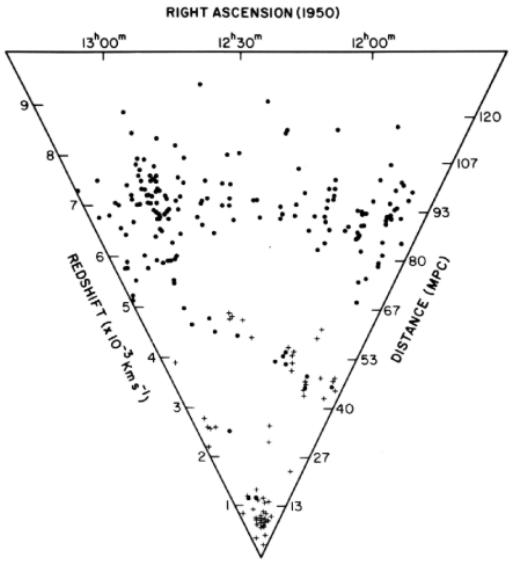

Figure 8: **Discovery of Voids in Galaxy Surveys.** Wedge diagram of the Coma/A1367 supercluster from Gregory & Thompson (1978), showing one of the earliest visual confirmations of voids in galaxy redshift surveys. The Coma cluster appears on the left, A1367 on the right, with a filament between them and a clear underdensity in the foreground.

into larger ones (the "void-in-void" process), while others collapse if embedded in overdensities (the "void-in-cloud") process (Sheth & van de Weygaert, 2004). These two mechanisms explain the diverse shapes and lifecycles of voids across cosmic time.

For comprehensive reviews on the physics, dynamics, and cosmological applications of voids, we refer the reader to van de Weygaert & Platen (2011a); van de Weygaert (2016a); Pisani et al. (2019); Cai & Neyrinck (2025).

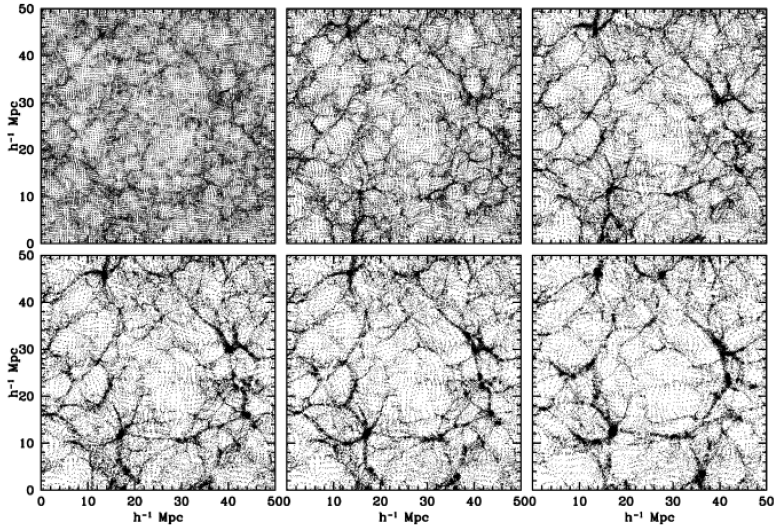

Figure 9: **The Two Modes of Void Evolution. Top:** Sequence from an N-body simulation showing the void-in-void process. **Bottom:** Snapshots of voids undergoing void-in-cloud process, with velocity vectors showing infall of surrounding matter. Adapted from van de Weygaert (2016b).

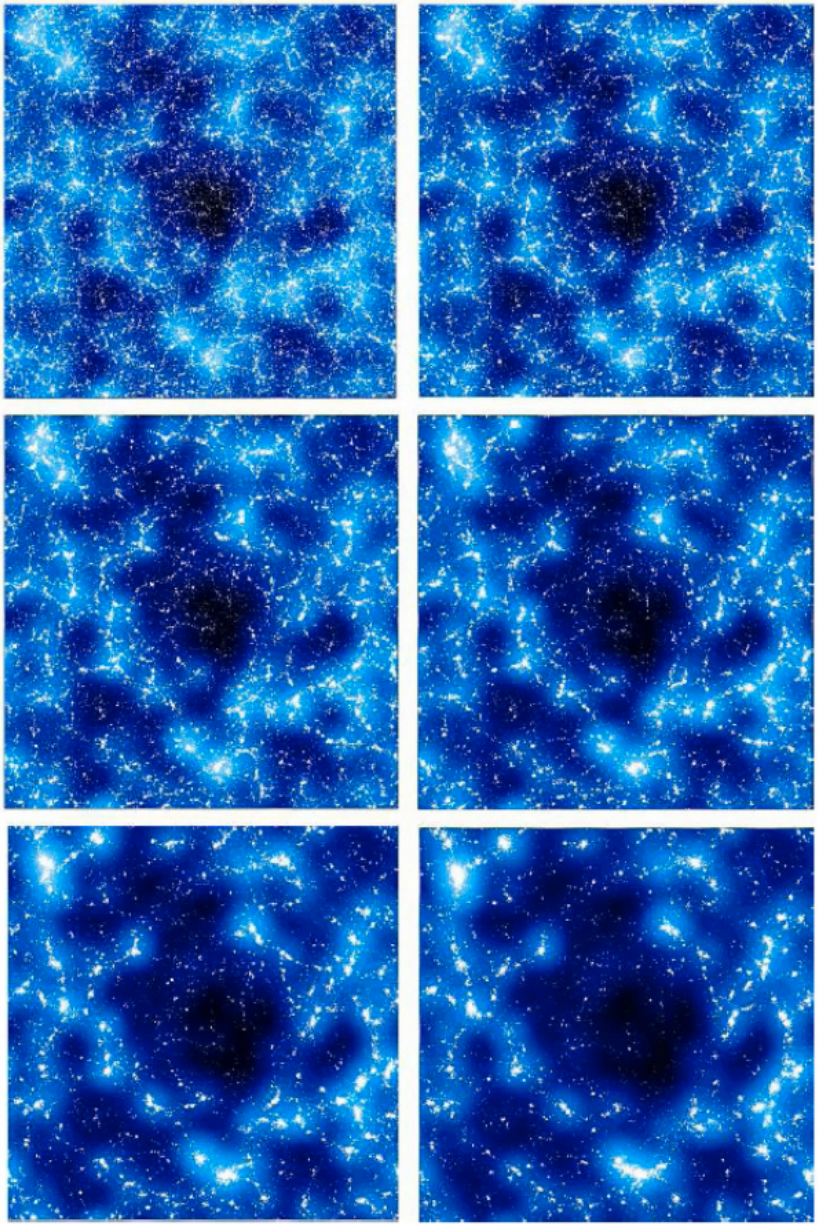

Figure 10: **Evolution of a cosmic void** Time sequence showing the expansion of a void in an $n = 0$ power-law ΛCDM model. Each panel depicts a slice 50 h^{-1}Mpc wide and 10 h^{-1}Mpc thick at six time steps ($a = 0.05$ to $a = 1.0$). The void empties out and expands, while surrounding filaments and walls become more pronounced. Adapted from van de Weygaert & Platen (2011b); Platen (2009).

Void Detection

A first comparative analysis of void detection techniques was conducted by (Colberg et al., 2008), following a conference series The authors compared thirteen various algorithms on a single ΛCDM simulation and showed enormous differences between the void finding algorithms. The comparison showed important difference in size, shape, and number of voids among the methods, and emphasized the importance of clearly declaring the void definition employed in any analysis.

Among the numerous techniques, the watershed transform is one of the most popular for void detection. The Watershed Void Finder (WVF) of (Platen et al., 2007) is an almost parameter-free algorithm that tries to identify voids directly from the density field without making any assumptions regarding their size or shape. It relies on the watershed transform, a mathematical segmentation method initially designed for image analysis, applied here to the continuous matter density field reconstructed from discrete tracers using Delaunay Tessellation Field Estimation (DTFE). The WVF devides the density field into individual basins around local minima, whose boundaries are defined by topological ridges. These individual basins are individual voids. The power of the WVF is that it is able to trace objectively the hierarchical and multi-level structure of underdensities in the cosmic web. As demonstrated by (Platen et al., 2008), the voids that are generated are physical: their orientation is related to the cosmic tidal field, as expected from theory.

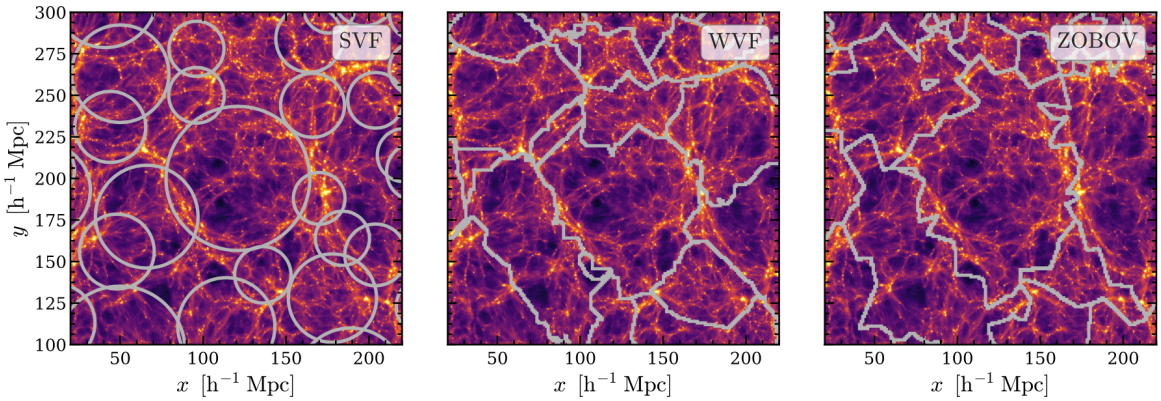

Figure 11: **A Visual Comparison of 3D Void-Finding Algorithms.** Grey contours indicate voids identified by three methods in a GR simulation snapshot at $z = 0$: spherical underdensity (SVF, left), watershed (WVF, center), and ZOBOV (right). The background shows the dark matter density field in a 50 h^{-1}Mpc thick slice along the z-axis of the simulation. Adapted from Paillas et al. (2019).

A similar yet not the same approach is ZOBOV (ZOnes Bordering On Voidness), introduced by (Neyrinck, 2008). Like WVF, it is based on the watershed concept, but operates on a density field reconstructed via Voronoi tessellation rather than Delaunay. ZOBOV also introduces a statistical procedure for estimating the significance of detected voids based on Poisson noise expectations. While its topological principle is similar to WVF, it is a simplified implementation, and the void regions it identifies may differ significantly depending on sampling and resolution. ZOBOV forms the basis of the VIDE toolkit, which extends the algorithm with post-processing and cataloging features.

Recent developments include the REVOLVER code by (Nadathur & Hotchkiss, 2015) and later improvements, which extend the watershed method by adding Voronoi-based density es-

timation and more complex void merging procedures. These advances have proven especially successful in generating robust void catalogs from observational data.

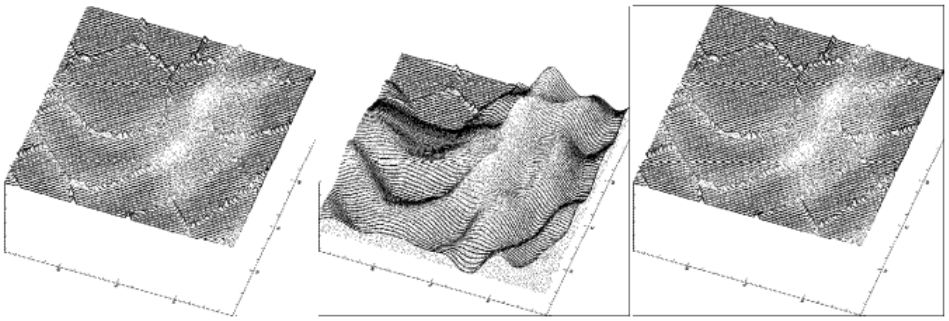

Figure 12: **Principle of the Watershed Transform.** Three frames illustrate how watershed-based void finders segment the cosmic density field. Adapted from Platen et al. (2007).

Beyond watershed-based approaches, a number of other void-finding methods have been developed. These comprise spherical underdensity void finders, which identify voids as spherical regions beneath a specified density threshold; excursion set-based models, which link void statistics to theory predictions through stochastic formalisms; and dynamical approaches, which follow void evolution founded on the displacement or velocity field, as opposed to density. Each of these approaches offers specific advantages depending on the structure of the data and the cosmological questions being addressed.

The existing void detection methods, both those specially created to be applied to projected galaxy surveys and weak lensing data, are comprehensively reviewed by (Cautun et al., 2018). Their analysis provides a detailed comparison of theoretical frameworks, practical implementations, and the relative performance of established algorithms across a range of observational contexts.

Cosmic Voids as Cosmological Laboratories

Though often regarded as empty, cosmic voids are among the most information-rich structures in the Universe. It is precisely their emptiness that renders them so useful: with fewer galaxies, less nonlinear structure, and less astrophysical feedback, voids develop in a regime of large-scale gravity and cosmic expansion. This relative simplicity allows for cleaner theoretical modeling than in overdense regions, where small-scale complexity can overwhelm cosmological signals.

Cosmic voids are sensitive probes of the underlying cosmology. Their shapes, sizes, and dynamics encode information about dark energy, dark matter, gravity, and the initial conditions of structure formation. They thus provide a complementary testing ground to traditional probes like the cosmic microwave background, galaxy clustering, and weak lensing (Pisani et al., 2019; Cai & Neyrinck, 2025).

One powerful cosmological application of voids is through their morphology and expansion, which are sensitive to the equation-of-state parameter of dark energy, w. Since voids expand faster than the cosmic average, they amplify tiny deviations in the expansion history, making them useful for constraining dynamical dark energy models (Lee & Park, 2009; Bos et al., 2012).

The Alcock-Paczyński (AP) test applied to stacked voids (Lavaux & Wandelt, 2010; Hamaus et al., 2014) exploits the fact that, on average, voids should appear spherical in comoving coordinates. Observed distortions in their angular versus radial dimensions thus constrain the

cosmological distance-redshift relation, providing estimates of the Hubble parameter $H(z)$ and angular diameter distance $D_A(z)$.

Void dynamics also constrain dark matter properties and alternative theories of gravity. Their underdense interiors, ruled by coherent outflows rather than random motions, are therefore great environments to constrain the growth rate of structure through redshift-space distortions (Hamaus et al., 2015). Modified theories of gravity such as $f(R)$ gravity and scalar-tensor theories give different predictions for void profiles via their screening mechanisms, which have been tested through simulations (Li et al., 2012; Llinares et al., 2014).

The void size distribution, or the number density of voids as a function of their effective radius, is one of the most sensitive cosmological void statistics. It is a direct probe of the primordial power spectrum and the Universe's matter content. This is encapsulated in the SvdW model (Sheth & van de Weygaert, 2004), a void counterpart of the Press-Schechter formalism. The model forecasts a peaked size function that was numerically verified in simulations by Platen et al. (2008). Void abundances have emerged as a premier observable for future surveys such as Euclid and DESI.

For a comprehensive overview of void-based cosmology, we refer the reader to Pisani et al. (2019); Cai & Neyrinck (2025).

Linear Theory and the Growth of Cosmic Voids

The early Universe had matter almost uniformly distributed with small density variations in the form of a Gaussian random field. Cosmic voids are the descendants of the most extreme minima of these fluctuations. The regions of underdensity expand and get emptier and larger over time, repelling the matter around them and imposing the formation of the cosmic web.

In the linear regime, the evolution of density perturbations is well described by a single growing mode:

$$\delta(\mathbf{x}, t) = D(t)\, \delta_0(\mathbf{x}), \tag{1}$$

where $\delta_0(\mathbf{x})$ is the initial density field and $D(t)$ is the linear growth factor. In an Einstein–de Sitter universe, this scales as $D(t) \propto a(t) \propto t^{2/3}$, reflecting how faster expansion causes structures to grow.

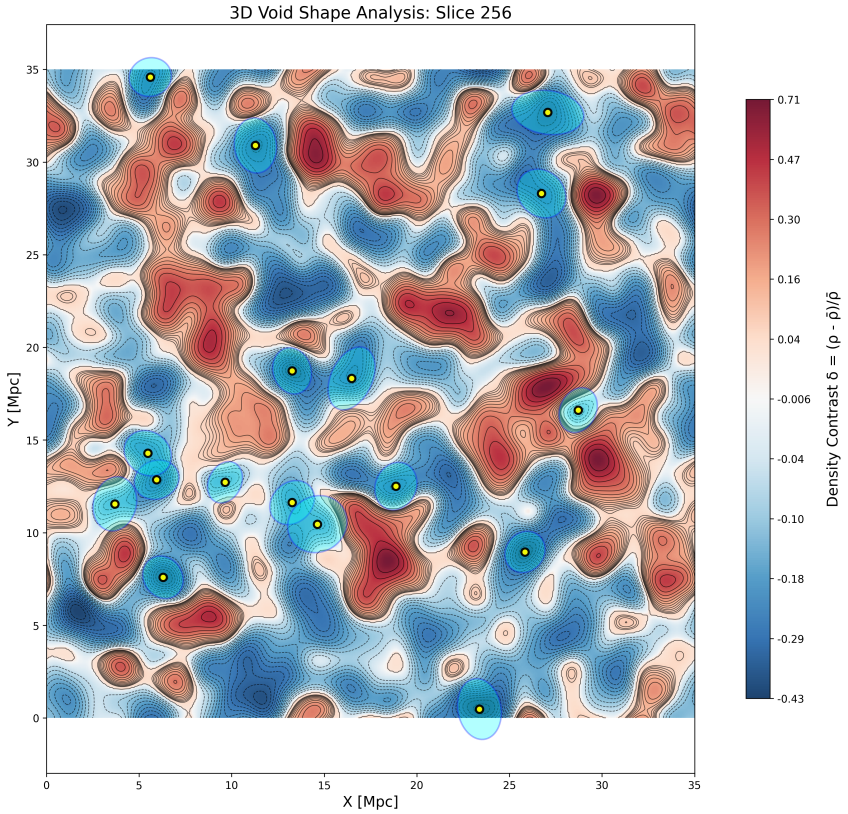

Figure 13: **Initial Gaussian density field with ellipsoidal fits.** Underdense regions in the initial density field are well described by ellipsoidal contours (blue). The ellipsoidal model assumes voids form around such minima, motivating its use for analytical modeling. Adaped from (**?**).

For voids, this linear growth lasts longer than for overdense regions since their formation goes through close to shell-crossing. The interiors of voids thus grow increasingly underdense and their edges develop rims of high density as material flows out.

Figure 13 shows a slice of an initial Gaussian density field, where the blue contours mark local minima. These initial conditions govern the shape and orientation of voids through the tidal field, setting the stage for their anisotropic expansion in nonlinear stages.

6 The Spherical Model of Void Evolution

The spherical model provides an analytically solvable framework to study the nonlinear evolution of cosmic voids. Although idealized, it is one of the few cases in which the full dynamics of a growing underdensity can be computed exactly prior to shell crossing. It assumes spherical symmetry, no shell-crossing, and neglects small-scale substructure, treating voids as concentric shells expanding independently under gravity. This model forms the theoretical basis for many empirical void definitions and is a cornerstone of our understanding of void dynamics (Gunn & Gott, 1972; Bertschinger, 1985; Sheth & van de Weygaert, 2004).

Basic Setup and Evolution

Each mass shell in the spherical model evolves as a mini-universe governed by its own Friedmann-like equation. The physical radius of a shell is given by:

$$r(t) = \mathcal{R}(t)\, r_i, \tag{2}$$

where $\mathcal{R}(t)$ is the local expansion factor and r_i the initial physical radius. The evolution is fully determined by the shell's initial density contrast and velocity.

To describe the evolution, two quantities are introduced: The effective density contrast of the shell compared to a critical universe:

$$1 + \Delta_{ci} = \Omega_i \left[1 + \Delta_i\right], \tag{3}$$

where Ω_i is the cosmic density parameter at time t_i, and Δ_i is the average density contrast within the shell.

The kinetic parameter α_i, which measures the deviation of the shell's velocity from pure Hubble flow:

$$\alpha_i = \left(\frac{v_i}{H_i r_i}\right)^2 - 1. \tag{4}$$

These parameters determine the dynamical class of the shell:

- **Closed shell** ($\Delta_{ci} > \alpha_i$): gravity dominates, and the shell eventually turns around and collapses.
- **Critical shell** ($\Delta_{ci} = \alpha_i$): the shell asymptotically slows without ever turning around—marking the threshold between collapse and unbounded expansion.
- **Open shell** ($\Delta_{ci} < \alpha_i$): the shell is underdense and expands forever.

This classification is very important: it shows that voids are naturally described by open shells. In particular, most voids exhibit $\Delta_{ci} < \alpha_i$, leading to perpetual expansion. Unlike in ellipsoidal models, the spherical framework is not restricted by homogeneity assumptions—its evolution depends only on the mass enclosed within radius r, enabling a full nonlinear treatment up to shell crossing (Sheth & van de Weygaert, 2004; van de Weygaert & Platen, 2011b).

Shell Crossing and Bucket Profiles

As a void evolves, ithe inwards shells expand more rapidly than the outwards shells because of the greater local underdensity. This eventually results in the shell crossing effect in which the inner shells catch up with the outer shells. This is the point of failure of the spherical model

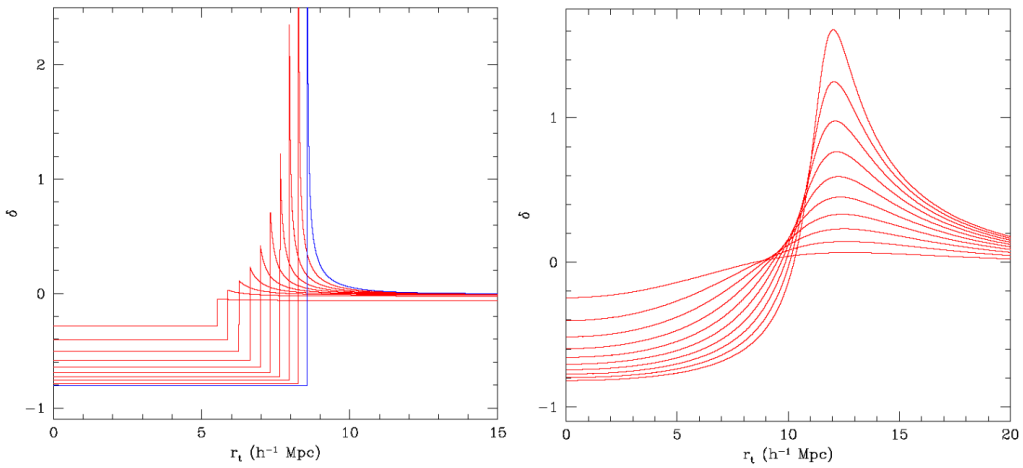

Figure 14: Time evolution of the density profiles of spherical perturbations. **Left:** Theoretical tophat underdensity before and during shell crossing. **Right:** Smoothed evolution into the characteristic "bucket-shaped" void density profile with a flat core and sharp ridge, produced by shell crossing and differential expansion. Adapted from Sheth & van de Weygaert (2004).

validity and the beginning of a non-linear regime featuring multi-streaming and ridge formation on the void boundary (Bertschinger, 1985; Fillmore & Goldreich, 1984).

The result is the emergence of a characteristic bucket-shaped density profile, shown in Figure 14. The left panel displays an idealized top-hat underdensity at various times, and the right panel displays the development of a smoother profile with an underdense core and a steep density ridge close to the void boundary. This morphology is universally observed in simulations and observations and is among the most stable features of nonlinear void evolution (Cautun et al., 2017; Hamaus et al., 2014).

Peculiar Velocities and Expansion Rates

The spherical model also predicts the velocity field inside voids. Before to shell crossing, the velocity is purely radial, with a super-Hubble outflow:

$$v_{\rm pec}(r,t) = H_u(t) r \left\{ \frac{g(\Theta_r)}{g(\Theta_u)} - 1 \right\}, \tag{5}$$

where $g(\Theta)$ is a known "velocity function" depending on the development angle Θ_r and the background cosmology.

After shell crossing, a self-similar phase emerges in which the void expands with a well-defined excess Hubble rate:

$$H_s = \frac{4}{3} H_u(t_{sc}), \tag{6}$$

indicating that voids expand faster than the background universe due to their negative density contrast.

On the Limits of the Spherical Model

Although the spherical model does yield an exact solution for spherically symmetric perturbations (up to shell crossing), it is not limited to homogeneous density profiles. Indeed, one of its

advantages is that it can be applied to arbitrary radial density and velocity profiles provided there is no shell crossing, and the evolution at a particular radius depends only on the enclosed mass. This also renders it an effective instrument for overdensity simulations, for which the gravitational collapse is generally isotropic and locally mass-dominated. The subsequent turnaround and collapse predictions match theory and simulations very accurately (Figure 14, left).

But this symmetry is a drawback for the case of voids. Underdense regions grow due to not just their inherent lack but also owing to their large-scale structure, i.e., tidal fields. The spherical model, by being limited to isotropic expansion, does not incorporate these anisotropic distortions, which are accountable for realistic void evolution.

Ellipsoidal models remedy this by permitting anisotropic expansion along three principal axes. They do assume a homogeneous interior, which is restrictive. For voids, however, this is a reasonable approximation: simulations show that the interiors of voids are extremely close to uniform density, so less versatile in profile shape but still reproducing key elements of void evolution, like the characteristic shape deformation, that the spherical model cannot.

This renders it better adapted to describe the real dynamics of cosmic voids (Sheth & van de Weygaert, 2004; **?**).

7 The Homogeneous Ellipsoidal Void Model

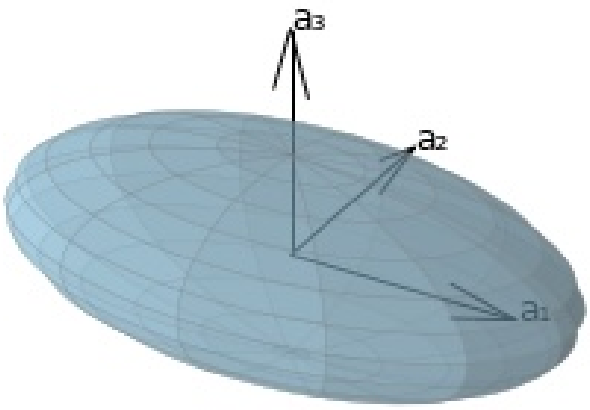

Figure 15: **Ellipsoidal Void Representation.** Three-dimensional visualization of a void modeled as a homogeneous ellipsoid, based on the computational implementation of the ellipsoidal evolution model developed in this work. The axes a_1, a_2, and a_3 represent the principal directions of expansion.

The homogeneous ellipsoidal void model extends the spherical approximation by allowing anisotropic expansion along three principal axes. Originally introduced by (Icke, 1984) and later expanded by (White, 1979; Eisenstein & Loeb, 1995; Bond & Myers, 1996; Desjacques, 2008), this model offers one of the most transparent and physically intuitive frameworks for understanding the nonlinear evolution of voids embedded in the cosmic web.

In contrast to overdense ellipsoids, which collapse rapidly along their shortest axes and quickly break the assumption of homogeneity, underdense regions tend to expand and flatten over time. As a result, their interiors evolve into nearly uniform, low-density regions, often described as having a "bucket-shaped" profile (van de Weygaert & Platen, 2011b; van de Weygaert, 2016b). This makes the homogeneous ellipsoidal model particularly well-suited for describing void dynamics, especially in the quasi-linear regime.

The dynamics of the expansion along each principal axis $R_m(t)$ (with $m = 1, 2, 3$) is governed by:

$$\ddot{R}_m = -4\pi G\bar{\rho}(1+\delta)\alpha_m R_m - \tau_m R_m + \frac{\Lambda}{3}R_m, \tag{7}$$

where each term encapsulates a distinct physical process driving the void's evolution.

Self-gravity and the α_m Coefficients

The first term in Eq. (13) describes the gravitational pull from the homogeneous interior of the ellipsoid. The geometric coefficients α_m modulate how strongly gravity acts along each axis and are determined by:

$$\alpha_m = R_1 R_2 R_3 \int_0^\infty \frac{ds}{(R_m^2+s)\sqrt{(R_1^2+s)(R_2^2+s)(R_3^2+s)}}, \tag{8}$$

with the constraint $\sum_{m=1}^{3} \alpha_m = 2$. These coefficients reflect the shape of the ellipsoid: in the spherical limit, $\alpha_m = 2/3$, reaching isotropic expansion. However, in a triaxial void, α_m differ along each axis, producing directional variation in gravitational acceleration. Since voids have $\delta < 0$, this term acts as a repulsive force, accelerating the void's expansion.

Tidal Forces Term (τ_m)

The second term in Eq. (13) accounts for external gravitational influences from the large-scale cosmic environment. The quantity τ_m is the eigenvalue of the tidal shear tensor, which describes the curvature of the external potential along the m-th principal axis. The tidal tensor is defined as the Hessian of the peculiar gravitational potential:

$$T_{ij} = \frac{\partial^2 \phi}{\partial q_i \partial q_j}, \tag{9}$$

where ϕ is the potential and q_i are Lagrangian coordinates. Since the tensor T_{ij} is symmetric by construction, it can be diagonalized, and its eigenvalues τ_1, τ_2, τ_3 correspond to the tidal accelerations along each axis.

In general, the tidal tensor takes the matrix form:

$$T_{ij} = \begin{pmatrix} \phi_{,11} & \phi_{,12} & \phi_{,13} \\ \phi_{,12} & \phi_{,22} & \phi_{,23} \\ \phi_{,13} & \phi_{,23} & \phi_{,33} \end{pmatrix}, \tag{10}$$

where $\phi_{,ij} = \partial^2 \phi / \partial q_i \partial q_j$.

In the special case of a quadratic gravitational potential, as in the Zeldovich approximation:

$$\phi(\mathbf{q}) = \frac{1}{2} \sum_{i=1}^{3} \lambda_i q_i^2, \tag{11}$$

the tidal tensor is already diagonal:

$$T_{ij} = \mathrm{diag}(\lambda_1, \lambda_2, \lambda_3), \tag{12}$$

so that $\tau_m = \lambda_m$. If all $\tau_m < 0$, the region expands along all axes and is classified as a void. If the signs of τ_m are mixed, the structure becomes anisotropic, forming sheets or filaments. A region with all $\tau_m > 0$ will collapse in all directions.

Because the density deficit of voids remains limited to $|\delta| < 1$, the influence of external tidal forces does not diminish with time, as it would for overdensities. As a result, voids remain highly sensitive to tidal shaping throughout their evolution. In extreme scenarios, anisotropic tidal fields may even lead to collapse along one or more axes, despite the void's initial underdensity (van de Weygaert & van Kampen, 1993). This term therefore captures how voids are stretched, squeezed, or distorted by their surrounding cosmic environment.

Dark Energy Term (Λ)

The final term introduces the repulsive influence of dark energy, modeled via the cosmological constant Λ. This contribution is isotropic and becomes increasingly dominant at late times when matter density is low. In void environments, where gravitational deceleration is weak, the effect of Λ ensures continuous expansion, aligning with observations of void growth in the late universe.

Why the Homogeneous Ellipsoidal Model is Well-Suited for Voids

The homogeneous ellipsoidal model is particularly effective for modeling cosmic voidsbecause of the physical characteristics of underdense regions. Voids, unlike overdense regions, which collapse into steeply grained, highly nonlinear peaks, expand over time and have flat, smooth interiors. As mass flows out of their centers, voids develop an effectively homogeneous density profile, which the ellipsoidal model's approximation of constant interior density accurately captures. This results in a typical super-Hubble outflow, in which the velocity profile is proportional to radius, a common result of the continuity equation for homogeneous expansion.

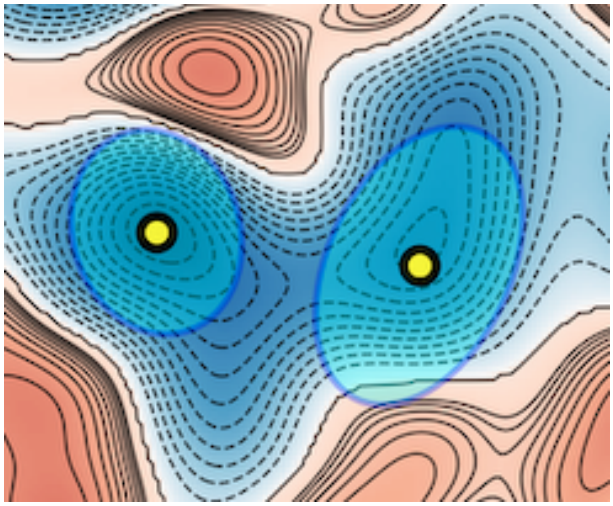

Figure 16: **Zoom-in on local density minima.** A close-up view of two underdense regions reveals how well the ellipsoidal contours approximate the surrounding density structure. The shape of the density well supports the assumption of a triaxial, homogeneous ellipsoidal geometry.Adapted from (Westerbroek, 2025)

Moreover, since voids typically originate from minima in the initial Gaussian density field, the surrounding density contours are well described by ellipsoidal surfaces. They align with the principal axes of the tidal field, making the ellipsoidal model grounded in the actual geometry of initial conditions. The benefit of this model is that even in the presence of anisotropic tidal forces, it remains predictive: tidal eigenvalues τ_m steer the shape evolution of voids, sometimes suppressing expansion along one or more axes, or in extreme cases, inducing axis collapse. These dynamics is captured by the full equation of motion in Eq. (13).

8 Computational Approach

To simulate the evolution of cosmic voids starting from the dynamical equations in Equation (13), this work develops a model designed for a homogeneous, isolated ellipsoidal underdensity. Built directly from theory, the model allows precise control over the three main physical influences on evolution: self-gravity, the cosmological background, and tidal fields. Each can be tuned independently or switched off entirely, making the framework both flexible and ideal for isolating the effects of individual forces on void dynamics.

8.1 Equations of Motion: Tracing the Expansion

The simulation is based on a system of six coupled second-order differential equations that govern the evolution of the principal axes $R_m(a)$, where $m = 1, 2, 3$. These equations generalize the spherical collapse model to ellipsoidal underdensities and incorporate the effects of anisotropic self-gravity, external tides, and dark energy:

$$\ddot{R}_m = -4\pi G\bar{\rho}(1+\delta)\alpha_m R_m - \tau_m R_m + \frac{\Lambda}{3}R_m, \tag{13}$$

The three terms correspond respectively to gravitational contraction along the m-th axis (modulated by the shape-dependent coefficient α_m), deformation from the external tidal tensor τ_m, and isotropic acceleration due to dark energy.

This formulation, implemented in `derivs.py`, extends the approach introduced by **?** to arbitrary cosmological backgrounds, enabling axis-by-axis evolution in an expanding universe.

8.2 Integrator Implementation

To evolve the axis dynamics of ellipsoidal voids as a function of the expansion factor, this model uses a leapfrog integrator implemented in `leapfrog_integrator.py`. The leapfrog method is chosen for its simplicity, stability, and compatibility with systems governed by second-order differential equations.

The script defines a custom integration routine that updates the axis lengths R_m and their derivatives $v_m = dR_m/da$ using the standard staggered leapfrog scheme:

$$v_m^{n+1/2} = v_m^n + \frac{\Delta a}{2} \cdot a''(R_m^n), \tag{14}$$

$$R_m^{n+1} = R_m^n + \Delta a \cdot v_m^{n+1/2}, \tag{15}$$

$$v_m^{n+1} = v_m^{n+1/2} + \frac{\Delta a}{2} \cdot a''(R_m^{n+1}), \tag{16}$$

where, Δa is the simulation step size and a'' is the axis acceleration derived from the evolution equation (8.1). The function takes initial axis values, velocities, and a user-defined acceleration model, returning the full evolution over a specified range of scale factors.

8.3 Simulation Pipeline

The simulation is organized in a modular structure, with `derivs.py` serving as the core component. This file implements the main physics governing the evolution of homogeneous ellipsoidal regions in an expanding universe, based on the dynamical equation in Eq. (8.1). It computes the

acceleration of each principal axis $R_m(a)$, incorporating three physical effects: self-gravity (via the ellipsoidal coefficients α_m), the cosmological background, and external tidal fields τ_m.

Within `derivs.py`, the system state is encapsulated in a class that tracks axis lengths, velocities, overdensity δ, and tidal forces. Its key routines include:

- `compute_alphas()`: calculates the shape-dependent coefficients α_m;
- `compute_accelerations()`: evaluates the full right-hand side of Eq. (8.1);
- `update_background()`: updates the cosmological background quantities $H(a)$ and $\bar{\rho}(a)$.

These functions are called at every timestep, ensuring consistency as the system evolves forward in scale factor.

Time integration is handled by `leapfrog_integrator.py`, which uses a second-order leapfrog method to update positions and velocities.

The overall simulation loop is managed by `leapfrog_style_sim.py`, which initializes the system, calls the integrator, and records the output. Initial conditions, including the density contrast δ_0, tidal eigenvalues τ_m, and axis configuration, are defined in `integration_initial_conditions.py` and passed to `derivs.py` at runtime.

The full simulation is run via `run_simulation.py`, which reads parameters from `simulation_parameters.py` and begins execution. Output is written to file and later processed using `postprocessing.py`.

Model Assumptions and Limitations

This model is designed to isolate the dominant physical mechanisms shaping the evolution of underdense ellipsoidal regions. To maintain interpretability and computational efficiency, several simplifying assumptions are made:

- **Homogeneity:** The interior of the void is treated as spatially uniform in density, with no internal gradients or substructure. This captures the average behavior while ignoring shell crossing or clumping.
- **Pressureless Matter:** The system consists of cold dark matter only, neglecting baryonic physics such as gas pressure or feedback.
- **No Rotation:** The principal axes of the ellipsoid remain aligned with the eigenvectors of the external tidal field throughout the evolution. Angular momentum and rotational deformations are not modeled.
- **Static Tidal Field:** External shear is imposed as a fixed, time-independent tensor in comoving coordinates. This captures large-scale anisotropic effects but omits tidal evolution or mode coupling.
- **Axisymmetric Configurations:** In the case of the tidal fields, symmetry is imposed on (e.g., $E_{mn} \propto \mathrm{diag}(-E, -E, 2E)$), simplifying the realistic evolution which could allow different configuartions.

While the model simplifies the outer regions by ignoring density gradients and interactions with surrounding structures, it remains well-suited for capturing the physics inside the void. In these central regions, where homogeneity is a reasonable assumption, the approach effectively tracks the key forces shaping void dynamic. Despite its idealizations, the model reproduces essential large-scale behaviors seen in more complex simulations, including the tendency toward sphericalization in isolation and directional collapse under strong shear. Its simplicity makes it both analytically sound and physically realistic for the inside of the voids.

Comparison with Cosmological Simulations

To test my theory-based simulation, I compare the model's predictions with a small set of underdense regions identified in a realistic cosmological context. These local minima in a smoothed Gaussian density field were extracted from the IllustrisTNG-3 Dark simulation by Luc Westerbroek, a fellow Bachelor student studying large-scale structure.

Each void serves as a reference point for evaluating the predictions of the ellipsoidal model. Although the model relies on simplified, idealized initial conditions to isolate specific physical effects, this setup makes it possible to compare its evolution directly with structures found in fully nonlinear N-body simulations.

To carry out this comparison, I computed the normalized axis lengths of the selected voids at three different redshifts. These measurements were then matched to corresponding stages in the evolution of the ellipsoidal model, allowing a direct, step-by-step comparison of shape changes over time.

In the final stage of this comparison, I compiled a table summarizing the predicted and simulated axis ratios across redshifts. This side-by-side evaluation provides a clear and quantitative check of the model's accuracy and reveals how closely its simplified assumptions predict the shape evolution of realistic cosmic voids.

Remarks on Model Scope

The ellipsoidal model developed in this work is intentionally simplified. Rather than aiming to reproduce the full complexity of cosmic voids in simulations, it provides a controlled framework for studying the effects of individual physical processes on void evolution.

A key strength of the model is its modular structure. Each physical contribution (self-gravity, dark energy, and external tidal forces) can be independently included or removed. For instance, setting $\tau_m = 0$ eliminates external shear, and excluding Λ isolates gravitational and background expansion effects. This structure makes it possible to isolate the role of each force in shaping voids, something not easily achievable in full N-body simulations where all effects act together.

Despite its idealizations, the model is adaptable to data-driven scenarios. Early-time configurations extracted from simulations can be used as nput for the model, which then evolves them forward under the assumptions of homogeneity and isolation. This makes it possible to follow how real voids might evolve over time by seeing how they respond to individual forces in a simpler setup.

9 The Illustris TNG50 Simulation

The IllustrisTNG project is an upgrade to the first Illustris simulation and a major breakthrough in the research of large-scale cosmological structure formation. It employs an advanced "next-generation" galaxy formation model that includes both refinements on previously established physics and entirely novel physical prescriptions. The research consists of a series of cosmological magnetohydrodynamical simulations that numerically solve for the coupled evolution of baryonic and dark matter in the ΛCDM model, using the AREPO code Springel (2010). AREPO is a quasi-Lagrangian second-order finite-volume solver with an unstructured Voronoi tessellation and moving mesh. Gravitational forces are computed with a hybrid TreePM method, and gas dynamics are solved using a directionally unsplit Godunov technique with magnetohydrodynamics Pakmor et al. (2011); Pakmor & Springel (2013). The resulting framework provides accurate, adaptive resolution over large ranges in density and spatial scale.

IllustrisTNG employs a physical model that has all of the primary processes thought to be responsible for galaxy formation and evolution. These include: (i) radiative heating and cooling of gas, including metal-line processes and an evolving UV background; (ii) star formation in the dense interstellar medium; (iii) chemical enrichment and stellar evolution by Type Ia and II supernovae, and by asymptotic giant branch (AGB) stars, after nine elements (H, He, C, N, O, Ne, Mg, Si, Fe); (iv) stellar feedback via kinetic galactic outflows; (v) supermassive black hole formation, accretion, and merging; and (vi) dual-mode black hole feedback, involving a thermal "quasar" mode and a kinetic "radio" mode depending on accretion state. The simulations also include primordial seed magnetic fields, which evolve self-consistently through ideal MHD Weinberger et al. (2017); Pillepich et al. (2018).

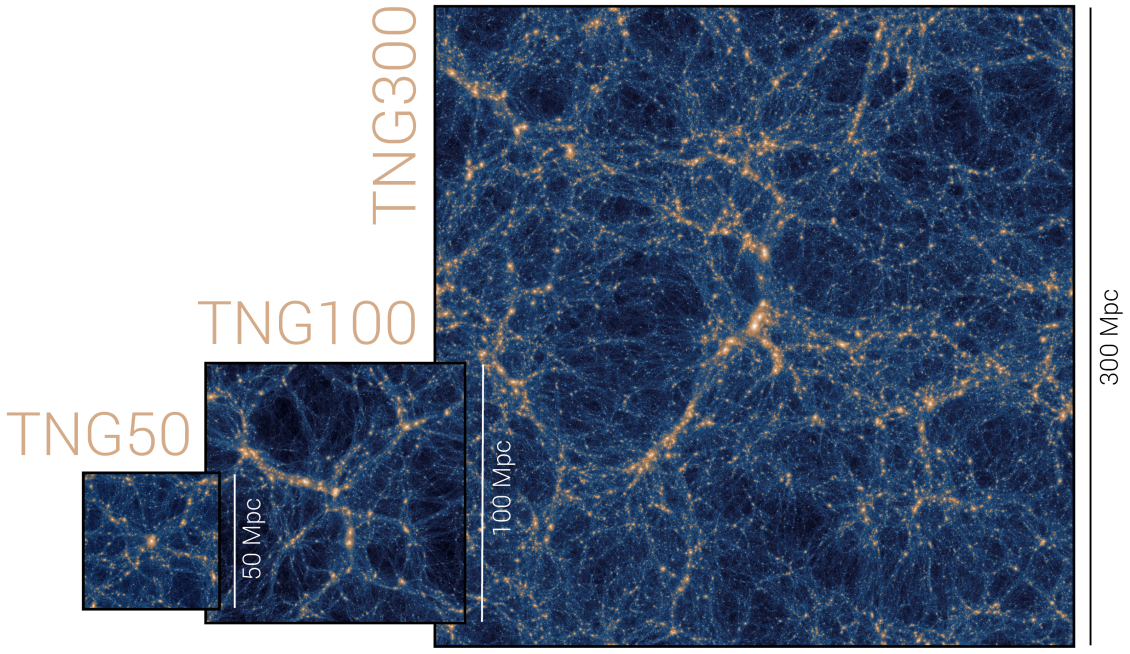

Figure 17: Comparison of the three TNG simulations: TNG50, TNG100, and TNG300. Each panel shows the projected dark matter density within the simulation volume. The three boxes are approximately but not exactly to scale. Image credit: IllustrisTNG Collaboration (IllustrisTNG Collaboration, 2024).

The simulation includes three primary volumes: TNG50, TNG100, and TNG300, corresponding to the comoving box scales of approximately 50, 100, and 300 Mpc, respectively. Every simulation has been run at several levels of resolution and has an associated dark-matter-only counterpart, which allows for detailed studies of baryonic effects. Of these, TNG50 stands out particularly with its record-breaking spatial resolution and cosmological volume. It follows the evolution of structure in a $(51.7\,\mathrm{Mpc})^3$ comoving box with 2×2160^3 resolution elements of gas and dark matter, with baryonic mass resolution of $8.5 \times 10^4\,M_\odot$ and dark matter mass resolution of $4.5 \times 10^5\,M_\odot$. The spatial resolution median for star-forming gas is 100–140 parsecs with a minimum gravitational softening of 74 comoving pc for gas and 288 pc (physical at $z = 0$) for stars and dark matter Nelson et al. (2019).

TNG50 simulates a statistically representative sample of galaxies at high resolution compared to current "zoom" simulations, enabling study of the small-scale galaxy structure (e.g., disks, spiral arms, bulges) and their large-scale cosmological context. Its ability to evolve the chemodynamical history of galaxies, halos, and the intergalactic medium over time makes TNG50 especially valuable for theoretical modeling and for interpretation of multi-epoch observational surveys.

The TNG simulations are given cosmological parameters that are consistent with Planck 2016 constraints and provide direct access to the time domain through hundreds of full snapshots. All simulation volumes are also run with the SUBFIND substructure finder Springel et al. (2001) and their evolutionary histories reconstructed through the SUBLINK merger tree algorithm Rodriguez-Gomez et al. (2015). The high fidelity, cosmological scale, and full physical modeling make TNG50 a critical benchmark for the testing of analytical models of void evolution and anisotropic structure formation.

9.1 Use of TNG50 Data in Void Ellipsoid Evolution

The second part of this thesis consists of a comparison of cosmological expectation for void evolution in the universe and results from realistic numerical simulations. For that purpose, I have used a data set based on the TNG50 simulation, generously provided by Luc Westerbroek, who is one of the Bachelor's students in our research group focused on voids in TNG50. His method is based on analyzing minima in the smoothed density field and determining their local geometry based on the Hessian matrix.

In this technique, the field of constant density was first smoothed by a Gaussian filter, and local minima were selected as possible void centers. For every minimum, the Hessian matrix of the density field was computed and diagonalized, yielding three eigenvalues $\lambda_1 \geq \lambda_2 \geq \lambda_3$ which express the curvature of the field in the principal directions. Assuming a Gaussian ellipsoidal profile, the respective semi-principal axes a_i of the void are estimated as

$$a_i \propto \frac{1}{\sqrt{\lambda_i}}.$$

Under this convention, λ_1 is the shortest axis and λ_3 the longest, offering a simple geometric interpretation for the shape of the underdensity.

The dataset that I utilized contains 100 such voids observed at three redshifts: $z = 20.05$, $z = 9.39$, and $z = 0.0$, thus witnessing void evolution from the early universe, through the reionization era, and into the present day. Owing to TNG50's high resolution and physical completeness, these voids preserve a true picture of cosmic structure formation involving both baryonic physics and dark matter.

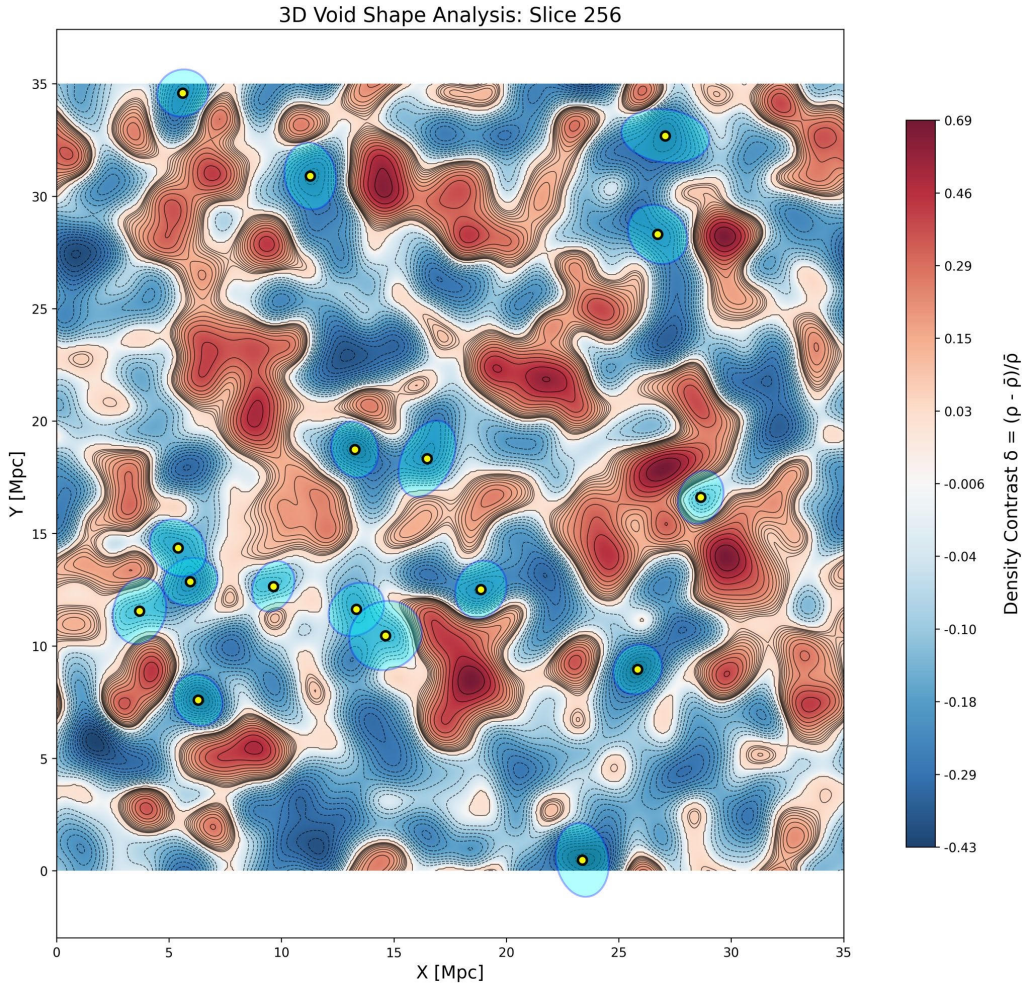

Figure 18: Density contrast map from the TNG50 simulation at slice index 256, as provided by Luuk Westerbroek. The color map represents the local density contrast $\delta = (\rho - \bar{\rho})/\bar{\rho}$, with underdense regions (voids) shown in blue and overdense regions in red. Superimposed are projected ellipsoids (in cyan) that represent selected voids from the catalogue. Each ellipsoid approximates the local geometry of a void, oriented according to its eigenvectors and scaled by the principal axis lengths derived from the deformation tensor. The yellow centers mark the identified minima of the density field. Adapted from (Westerbroek, 2025)

For this thesis, I use the axis lengths of these to track the void shapes as functions of time by computing the axis ratios a_3/a_1 and a_2/a_1 at each redshift. This allows quantitative comparison with the previously established ellipsoidal void model on idealized assumptions: isolated, homogeneous underdensities that develop in ellipsoidal symmetry. The voids in TNG, however, develop and evolve in a very anisotropic large-scale environment that is highly complex. Together, the two offer a helpful check on the robustness and realism of the analytic model.

10 Spherical Model: Structure and Evolution

As a first test of the numerical model, the simulation is run on a simple and symmetric case: the collapse of a spherical overdensity in an expanding Einstein–de Sitter universe. This setup excludes both dark energy and tidal forces, creating a clean environment to study the core features of nonlinear gravitational instability. Its analytical solution is well known, making it a reliable test for checking the accuracy and behavior of the code.

subcaption

10.1 Model Setup and Initial Conditions

The system is evolved using a self-gravitating collapse model based on the ellipsoidal framework, but initialized with perfectly spherical conditions. All three principal axes are set equal to $(1.0, 1.0, 1.0)$, and the initial density contrast δ_0 is varied over a representative range. In this symmetric setup, the ellipsoidal model reduces exactly to the standard Spherical Collapse Model, which describes the evolution of concentric, uniform shells in a universe with no tidal fields or dark energy.

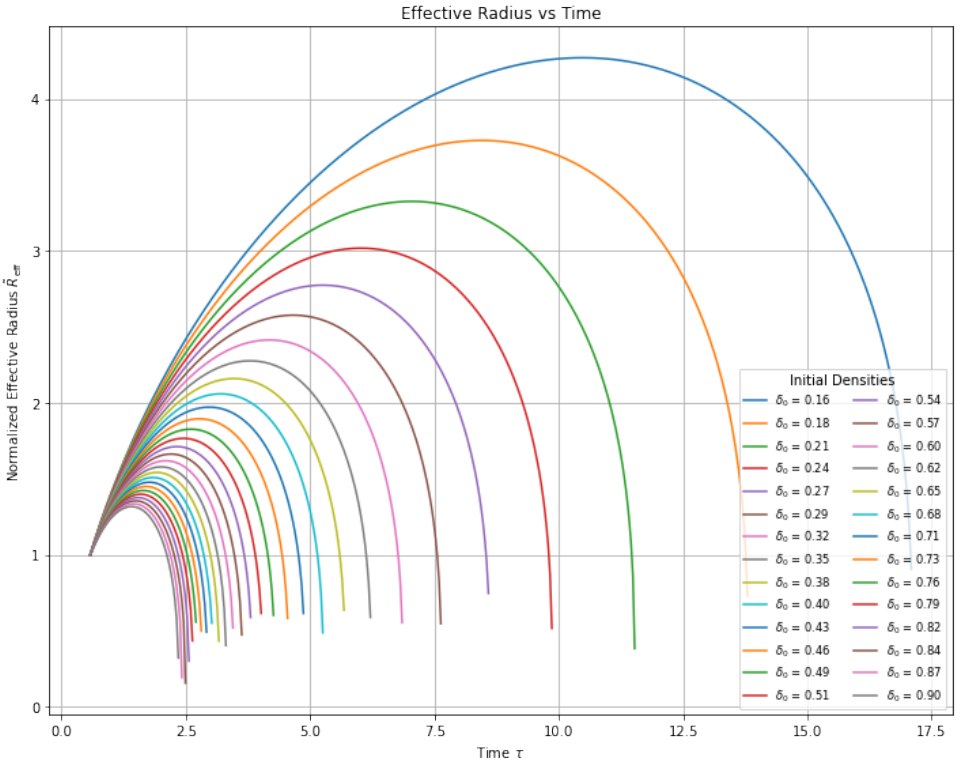

Figure 19: **Evolution of the normalized effective radius $R_{\rm eff}$ as a function of cosmic time τ.** The model shows how spherical overdensities with different initial contrasts δ_0 evolve. Larger overdensities collapse faster due to stronger self-gravity, while smaller ones remain expanding over the observed timeframe.

Figure 19 illustrates the nonlinear evolution of the normalized effective radius $R_{\rm eff}$ as a function of cosmic time τ, for a set of 30 spherical overdensities with initial density contrasts in the range $\delta_0 = 0.16$ to 0.90. The effective radius is defined as the geometric mean of the three

principal axes,

$$R_{\text{eff}} = (a_1 a_2 a_3)^{1/3}\,, \tag{17}$$

which, under spherical symmetry, provides a scalar measure of the size. Each plot is normalized to unity at the initial time($a \approx 0$).

At early times, all configurations follow the background Hubble expansion. As self-gravity becomes increasingly dominant, the initial expansion slows, reaches a maximum extent, known as the turnaround point, and subsequently reverses into collapse. In the parametric formulation of the Spherical Collapse Model, this turnaround occurs at a development angle of $\Theta = \pi$.

These results are consistent with the analytical predictions of the Spherical Collapse Model, which describes the evolution of a spherical overdensity through a parametric development angle Θ. In this formulation, the physical radius and cosmic time evolve as $R(t) \propto (1 - \cos\Theta)$ and $t \propto (\Theta - \sin\Theta)$, respectively. The system undergoes an initial expansion, reaches a maximum radius at $\Theta = \pi$ (the turning point), and subsequently reverses to collapse. At this stage, peculiar velocities vanish, and the influence of self-gravity becomes dominant. The formal collapse is achieved at $\Theta = 2\pi$, which corresponds to a vanishing radius in the idealized model.

Higher initial density contrasts ($\delta_0 \gtrsim 0.5$) reach this turnaround earlier and collapse more rapidly, while lower contrasts keep expanding throughout the simulation window ($a \leq 1$). This behavior illustrates the model's central principle: the evolution of a spherical overdensity is fully determined by its initial conditions. As δ_0 increases, the gravitational pull becomes sufficient to overcome the Hubble expansion at earlier times, leading to earlier decoupling and contraction.

The plot also highlights the limitations of linear theory for this configuration. At early times ($a \lesssim 0.3$), the evolution of the effective radius follows a nearly linear trend, consistent with linear growth predictions. However, significant deviations emerge as the system enters the nonlinear regime. Unlike linear theory, which predicts unbounded growth, the spherical model captures the finite-time turnaround and eventual collapse. The resulting contraction is continuous and smooth, reflecting the full nonlinear dynamics governed by the self-gravitating evolution of the mass shell.

10.2 Turnaround Time

Building on the evolution curves presented in Figures 19, the turnaround point is now examined. This moment marks the transition from expansion to contraction, defined by the vanishing of peculiar velocities and the onset of self-gravitational dominance. Within the parametric framework of the Spherical Collapse Model, turnaround corresponds to a development angle of $\Theta = \pi$, at which the overdense region reaches its maximum physical radius. The timing of this transition varies systematically with the initial density contrast δ_0.

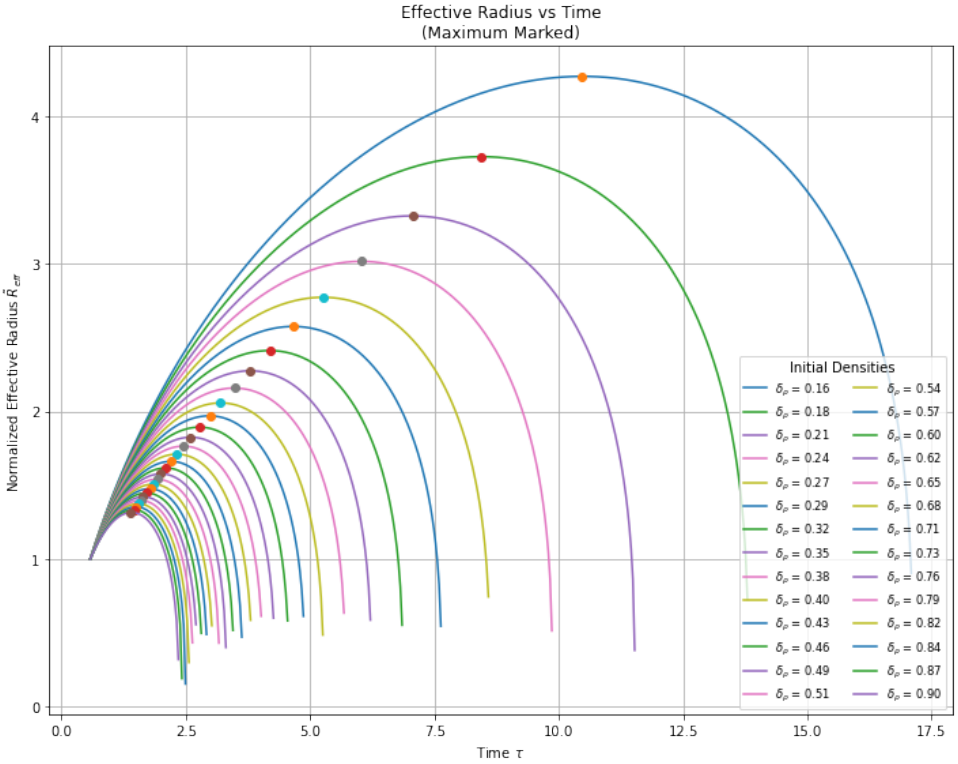

Figure 20: Evolution of the normalized effective radius R_{eff} versus cosmic time τ, with maxima marked for each overdensity. The dots indicate the turnaround points, i.e., the moment when expansion halts and collapse begins.

Each curve in figure 20 shows the evolution of R_{eff} over cosmic time τ, with turnaround points marked for each initial overdensity δ_0. Compared to the expansion-factor view in Figure **??**, this time-based representation makes it easier to see how collapse timing depends on initial conditions. The curves closely follow the analytical behavior of spherical mass shells described by the development angle $\Theta(t)$ in the Spherical Collapse Model.

Table 2: Maximum R_{eff}, $a_{\max}$, and $\tau_{\max}$ for each δ_0

δ_0	$\tau_{\max}$	$a_{\max}$	$R_{\text{eff}}^{\max}$
0.16	10.4626	0.6899	4.2707
0.18	8.4430	0.5980	3.7264
0.21	7.0612	0.5308	3.3253
0.24	6.0337	0.4780	3.0175
0.27	5.2542	0.4359	2.7740
0.30	4.6519	0.4019	2.5765
0.60	2.1009	0.2366	1.6182
0.90	1.3923	0.1798	1.3166

Table 2 lists the corresponding numerical values of the turnaround time $\tau_{\max}$, scale factor $a_{\max}$, and maximum radius $R_{\text{eff}}^{\max}$ for a representative set of initial overdensities.

The trends are striking and consistent with the analytic expectations:

- Collapse time is highly sensitive to δ_0: A small increase in initial overdensity results in a significantly earlier turnaround. For example, increasing δ_0 from 0.18 to 0.30 shortens the collapse time $\tau_{\max}$ by nearly 4 units. This reflects the exponential sensitivity typical of nonlinear gravitational systems.
- Collapse occurs from smaller radii at higher δ_0: Larger overdensities decouple from the background sooner and reach a smaller maximum radius before reversing. This is a natural outcome of stronger self-gravitational binding.

Dependence of Turnaround Time on Initial Overdensity Figure 21 shows how the turnaround time $\tau_{\max}$ depends on the initial density contrast δ_0, based on values measured from the simulation. Each blue point marks the peak of a specific $R_{\text{eff}}(\tau)$ curve, which is the moment when expansion stops and collapse begins. The trend is clear. Denser regions collapse earlier, since stronger self-gravity pulls them back faster.

The orange curve is a nonlinear fit that captures the shape of this relationship. For low values of δ_0, collapse takes a long time, reflecting weaker gravitational binding. As δ_0 increases, the turnaround time drops quickly and begins to level off. This matches the prediction from the Spherical Collapse Model, where the development angle $\Theta = \pi$ marks the maximum radius before collapse.

This plot highlights how sensitive collapse timing is to initial conditions. Even small changes in δ_0 lead to large differences in when structures stop expanding. That sensitivity is a core feature of nonlinear gravitational evolution.

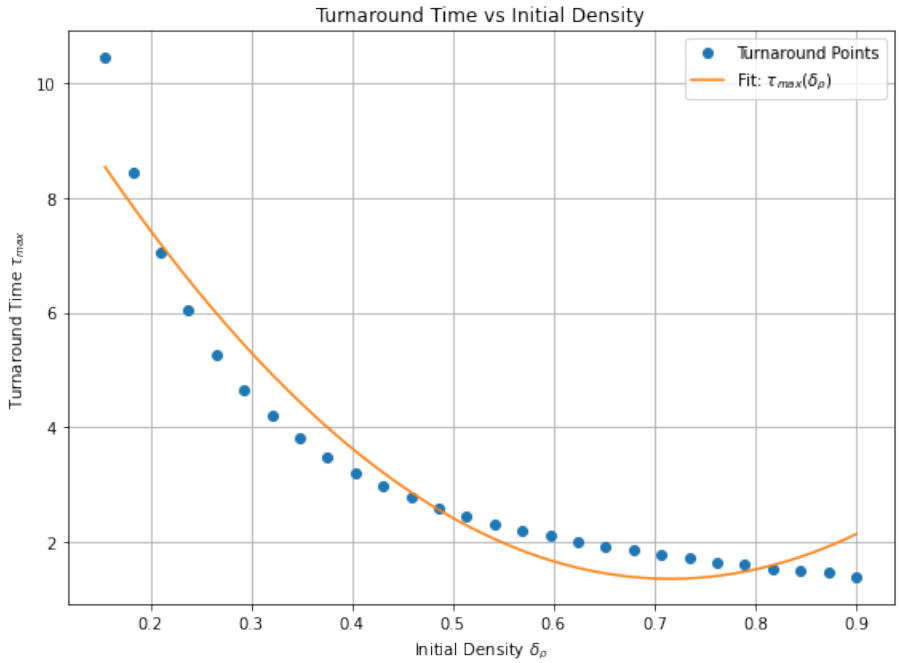

Figure 21: Turnaround time $\tau_{\max}$ as a function of initial overdensity δ_0. Blue points are simulation values based on the maxima of $R_{\text{eff}}(\tau)$. The orange curve is a smooth fit capturing the inverse dependence and flattening at high δ_0.

10.3 Peculiar Velocity Evolution

Peculiar velocities quantify motion relative to the Hubble flow. These velocities trace how gravitational forces act over time, providing a dynamic perspective that complements the previously examined structural quantities.

In Figure 22, the component velocities v_1, v_2, and v_3 are plotted against the expansion factor a for a range of initial overdensities δ_0. Their near-identical evolution reflects the isotropy of the initial conditions; any deviation observed at later times is a result of nonlinear internal dynamics rather than imposed anisotropy. A more integrated view is offered in Figure 23, where the total peculiar velocity v_{pec} is shown for each case, emphasizing the net infall driven by self-gravity.

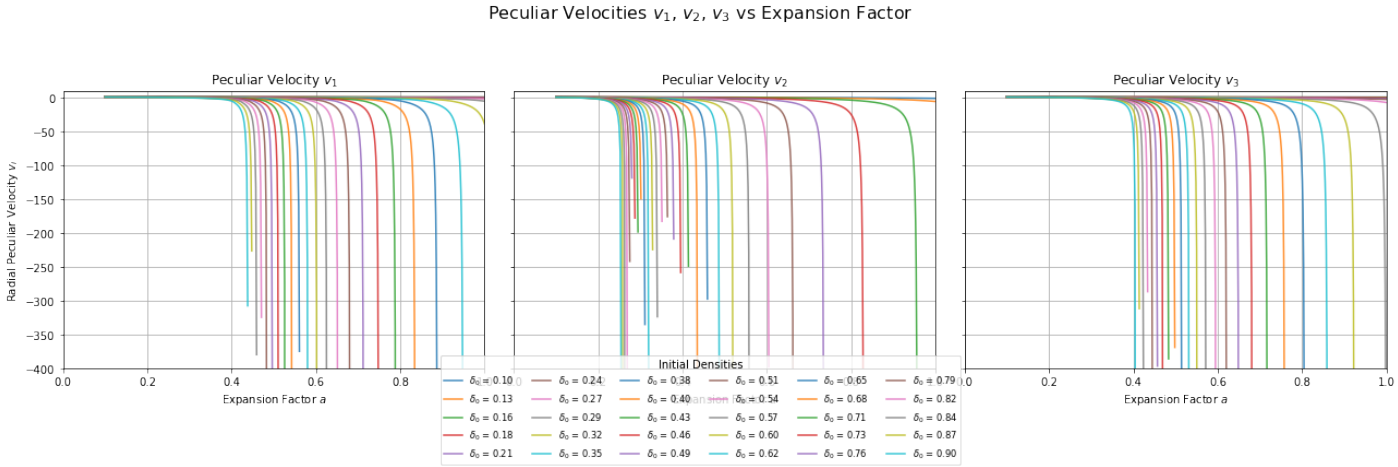

Figure 22: **Peculiar velocity components v_1, v_2, and v_3 versus scale factor a.** These velocities correspond to the principal axes of ellipsoidal overdensities with various initial contrasts δ_0. The curves illustrate how different axes undergo gravitational infall, with higher δ_0 regions experiencing earlier and more rapid collapse, indicated by sharply diverging velocity profiles.

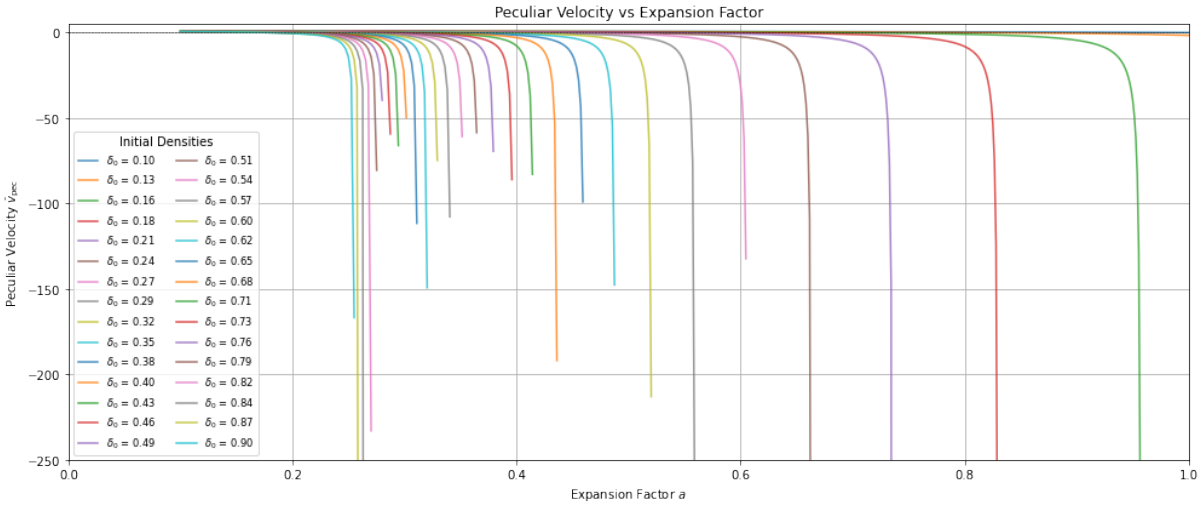

Figure 23: **Total peculiar velocity versus scale factor a.** This plot shows the combined infall velocity of the collapsing region. The transition to negative velocity marks gravitational decoupling and the onset of nonlinear collapse.

The peculiar velocity plot shows how nonlinear gravitational collapse shapes the system's dynamics. Early on, velocities stay close to zero, mirroring the background Hubble expansion. As self-gravity takes over, they quickly turn negative, and the collapse starts . This transition happens sooner and more sharply for higher initial overdensities, in line with the earlier turnaround times and the behavior of the effective radius.

10.4 Axis Evolution and Peculiar Velocities for a Single Overdensity

A single overdensity with initial contrast $\delta_0 = 0.13$ was also examined to better visualize the internal evolution of collapsing structures. Figure 24 plots the evolution of its three principal axes (a_1, a_2, a_3) and their corresponding peculiar velocities (v_1, v_2, v_3) over cosmic time τ.

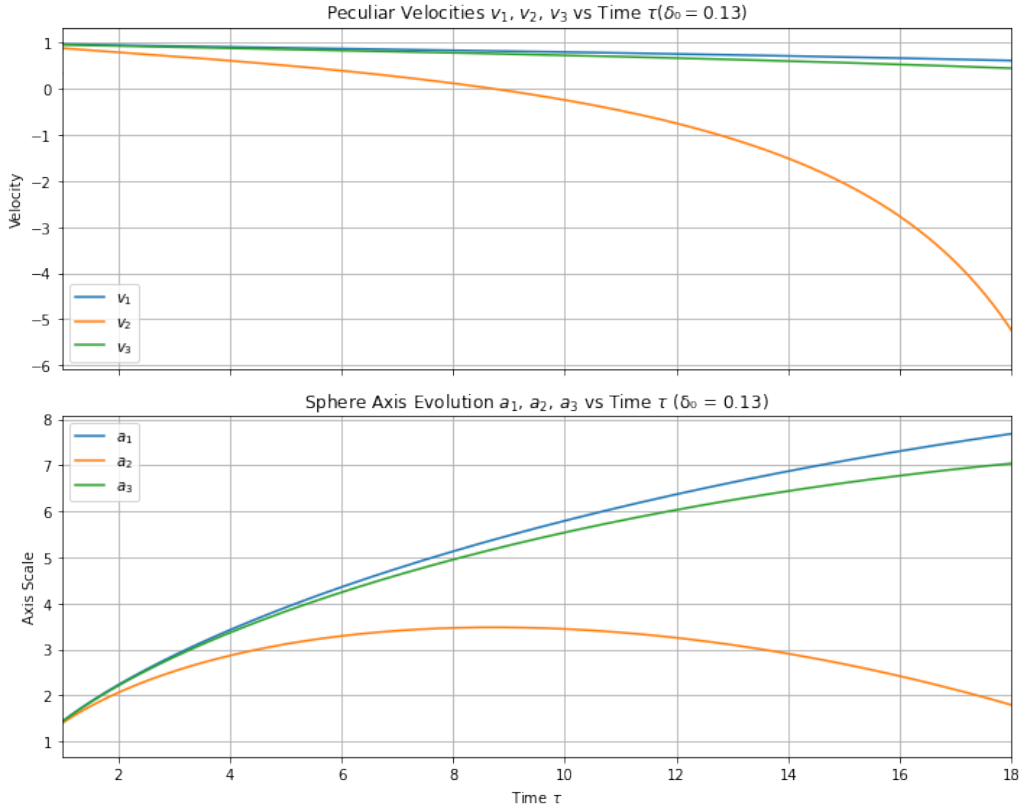

Figure 24: **Top: peculiar velocities v_1, v_2, v_3 for $\delta_0 = 0.13$ as functions of cosmic time τ. Bottom: evolution of the three ellipsoidal axes a_1, a_2, a_3.** Collapse occurs first along axis a_3, while a_1 and a_2 continue expanding longer, revealing the emergence of anisotropy during evolution.

Starting from nearly spherical conditions, the overdensity evolves into a clearly anisotropic configuration. As shown in Figure 24, all three axes initially expand together, but diverge as nonlinear effects take hold. Axis a_3 reverses first and collapses, followed by a_2, while a_1 continues to grow.

The top panel, showing peculiar velocities v_1, v_2, and v_3, reinforces this interpretation. Each velocity component becomes negative at different times, in accordance with the order of axis collapse.

10.5 Consistency with Classical Collapse

The spherical collapse results presented in this chapter confirm that the numerical model successfully reproduces the classic predictions of the Spherical Collapse Model. From turnaround timing and collapse behavior to peculiar velocity evolution and shape deformation, the simulations capture the full nonlinear dynamics of structure formation under idealized, symmetric conditions. Even when starting from perfect spherical symmetry, overdensities evolve into triaxial shapes driven entirely by self-gravity.

11 Ellipsoidal Model: Structure and Evolution

This section investigates the evolution of ellipsoidal underdensities (voids) in an expanding Einstein–de Sitter universe, focusing on a scenario governed exclusively by self-gravity. The systems are initialized with a uniform negative density contrast ($\delta_0 < 0$) and evolve in the absence of external tidal forces. Despite its idealized nature, this setup highlights key features of void dynamics, particularly the influence of gravitational rarefaction on both expansion and shape evolution.

11.1 Self-Gravity-Driven Evolution

To isolate the effect of self-gravity, a homogeneous ellipsoidal underdensity is evolved from initial conditions with no external tidal field. The background cosmology is Einstein–de Sitter, with $\Omega_{\rm m} = 1$ and $\Lambda = 0$. The simulation starts at scale factor $a = 0.1$ and runs until $a = 1$. The initial axis lengths are set to $(a_1, a_2, a_3) = (1.0, 0.9, 0.8)$, representing a mildly ellipsoidal void.

Effective Expansion Figure 25 displays the normalized effective radius $R_{\rm eff}$ as a function of expansion factor a, for different values of initial underdensity δ_0. Initially, all voids expand at the background rate. Over time, weaker self-gravity causes these regions to decouple from the Hubble flow and expand faster. More negative δ_0 values accelerate this divergence, illustrating how rarefaction amplifies with underdensity strength.

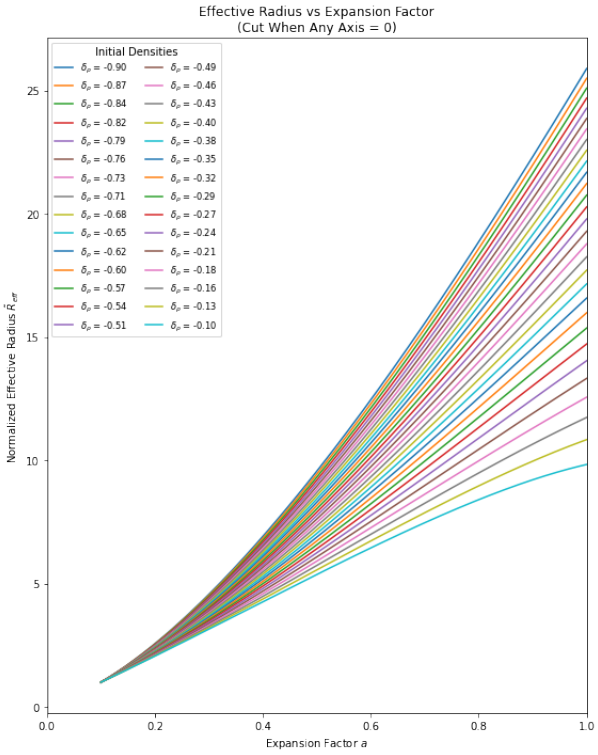

Figure 25: Evolution of the normalized effective radius $R_{\rm eff}$ for ellipsoidal underdensities with varying initial density contrast $\delta_0 < 0$. Greater underdensities expand more rapidly due to reduced self-gravity.

11.2 Comoving axis and Shape evolution

To analyze internal geometry, the evolution of axis lengths and ratios is tracked in comoving coordinates. Figure 2627 presents these results for a representative void with $\delta_0 = -0.9$ and initial axis lengths $(1.0, 0.9, 0.8)$.

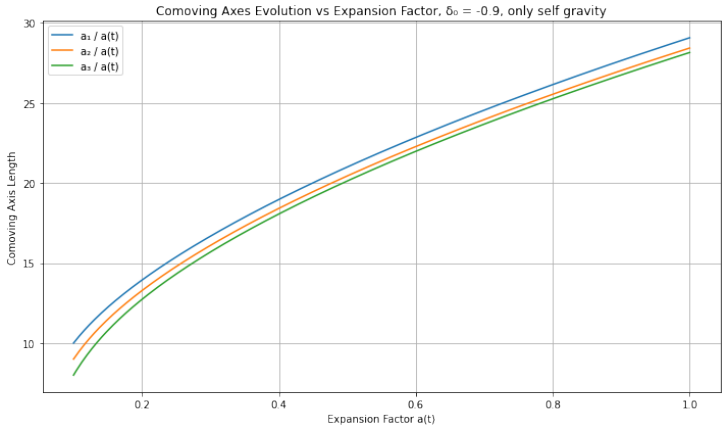

Figure 26: Comoving axis evolution for an isolated ellipsoidal void with $\delta_0 = -0.9$. The initially anisotropic configuration evolves as the axes converge over time.

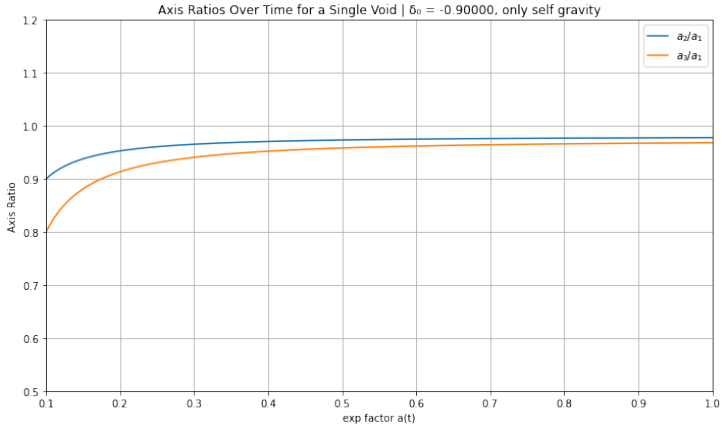

Figure 27: Axis ratios a_2/a_1 and a_3/a_1 for the same void. The increasing ratios indicate that the ellipsoidal shape becomes more isotropic, trending toward symmetry.

Figure 2627 illustrates the evolution of an initially anisotropic underdensity with $\delta_0 = -0.9$ in a self-gravitating, isolated setting. The left panel shows the comoving lengths of the three principal axes (a_1, a_2, a_3) as functions of the cosmological scale factor a. While the axes begin with different values, they converge over time, reflecting a gradual reduction in anisotropy. The right panel plots the axis ratios a_2/a_1 and a_3/a_1, which increase monotonically and asymptotically approach unity. This behavior indicates that the void becomes increasingly spherical as it expands, despite starting from an ellipsoidal configuration. The result highlights the symmetrizing effect of internal gravitational dynamics in isolated void evolution.

The geometric evolution is further illustrated in axis-ratio space. Figure 28 tracks the system's trajectory toward the spherical limit. Although the void remains slightly ellipsoidal throughout, its shape steadily converges toward $(b/a, c/a) = (1, 1)$.

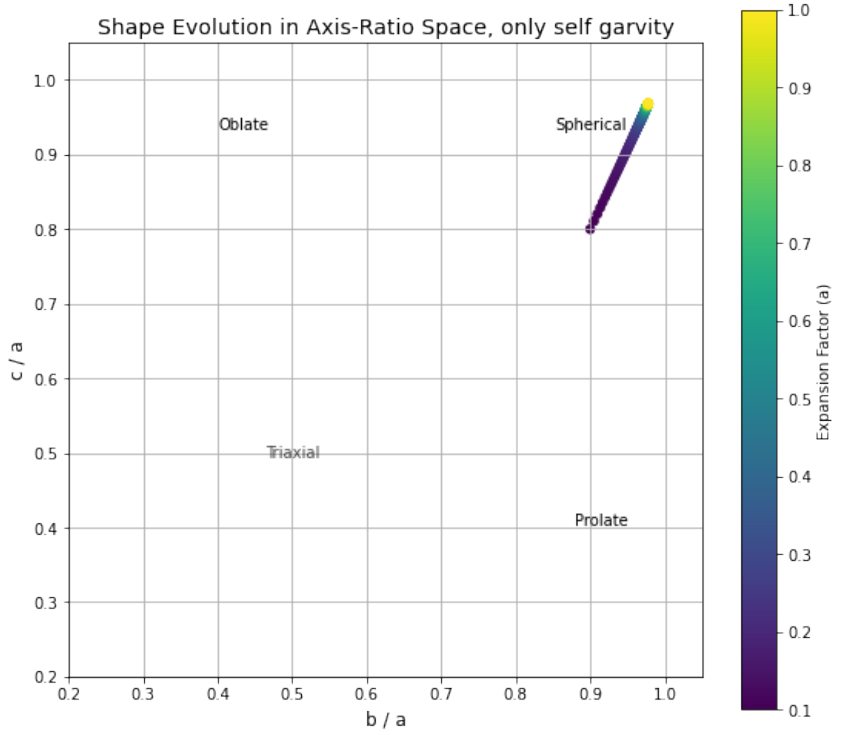

Figure 28: Axis-ratio trajectory for the same underdensity. Color encodes the expansion factor a. The shape evolves toward the spherical corner, confirming that gravitational rarefaction promotes isotropization in voids without external tides.

To provide an intuitive summary, Figure 29 presents 3D renderings of the void at three distinct expansion factors. The transformation from an initially triaxial ellipsoid to a nearly spherical geometry is clearly visible, along with the rapid increase in volume.

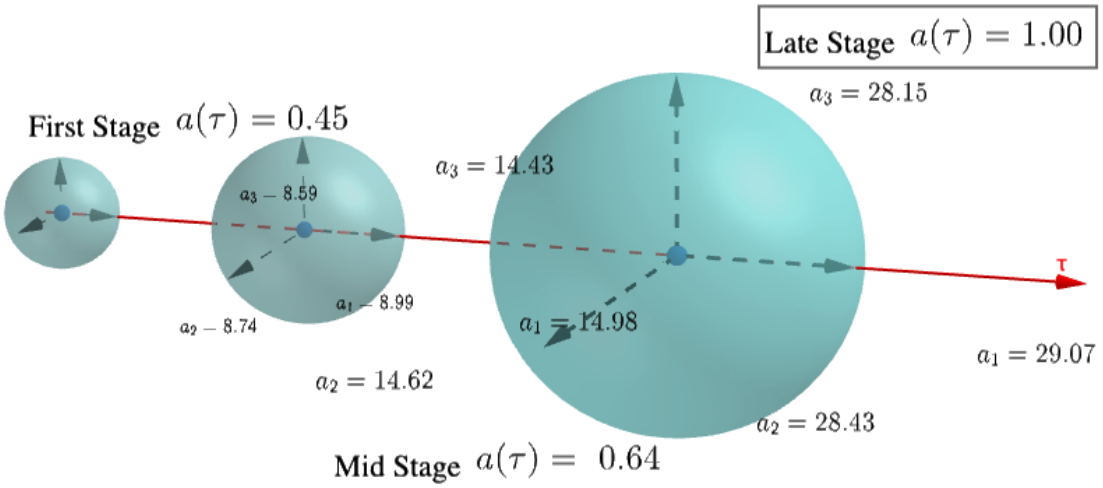

Figure 29: 3D snapshots of the void with $\delta_0 = -0.9$ at three expansion factors. Axis lengths are annotated. As time progresses, the void expands significantly and its shape becomes more spherical.

11.3 Interpretation

In this configuration, self gravity generates both rapid expansion and progressive shape symmetrization. Underdense regions initialized with ellipsoidal geometries evolve toward spherical symmetry over time. This trend is clearly reflected in the convergence of principal axes and the steady increase of axis ratios toward unity, as shown in Figure **??**. The expansion reduces initial anisotropies, leading to a final configuration that is significantly more isotropic than the starting state.

This behavior stands in sharp contrast to the evolution of overdense regions, where anisotropies typically grow as collapse proceeds. In those cases, gravitational amplification tends to exaggerate initial shape differences, often producing triaxial or filamentary structures. For voids, by contrast, the dynamics favor isotropization. This smoothing effect is a direct consequence of the repulsive nature of underdense gravitational fields in comoving coordinates, which dampen shear and suppress directional imbalances.

11.4 Impact of Dark Energy on Void Evolution

Having examined the evolution of isolated voids under the influence of self-gravity alone, we now investigate how this behavior changes when a cosmological constant $\Lambda > 0$ is introduced. Dark energy, modeled here via a repulsive Λ-term with $\lambda = 0.1$, accelerates the late-time expansion of the universe. It is natural to ask: does this accelerated expansion enhance anisotropies in void shapes, or does it reinforce the isotropization observed in the self-gravitating case?

We simulate the evolution of a triaxial ellipsoidal underdensity with initial density contrast $\delta_0 = -0.9$ and axis ratios $(a_1, a_2, a_3) = (1.0, 0.9, 0.8)$ in a universe with both matter and dark energy. The evolution of the three principal axes is shown in Figure 30. Compared to the $\Lambda = 0$ case, all axes grow substantially more due to the accelerated expansion induced by dark energy. However, their relative ordering and separation remain nearly unchanged throughout the simulation.

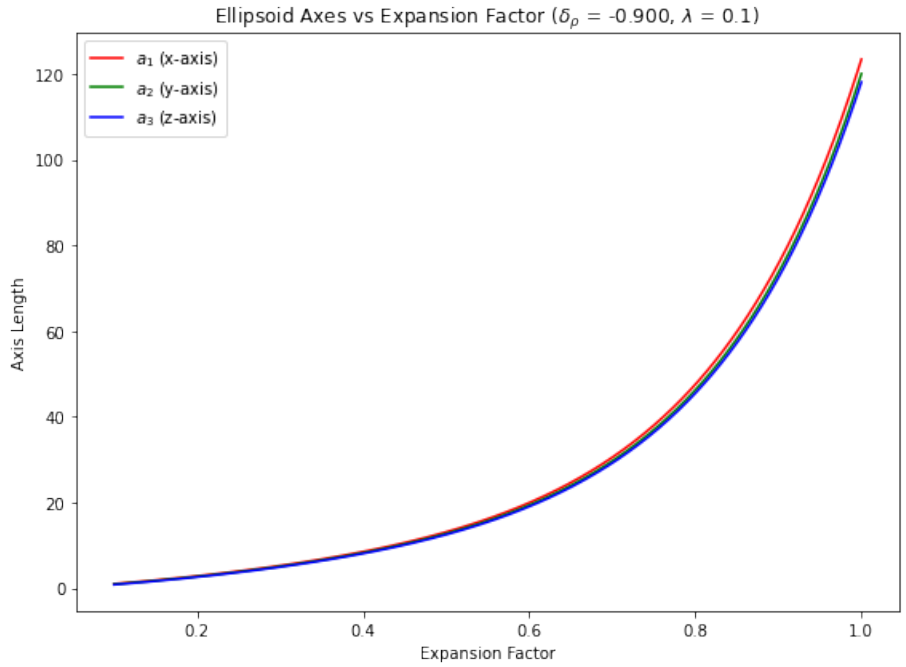

Figure 30: Evolution of ellipsoidal axes for a void with $\delta_0 = -0.9$ and a dark energy term $\lambda = 0.1$. All three axes expand more rapidly than in the self-gravitating case, but the relative growth rates remain coherent, indicating the absence of shape distortion.

To quantify the shape evolution, we examine the axis ratios a_2/a_1 and a_3/a_1 in Figure 31. Both ratios increase over time and approach values close to unity, just as in the purely gravitational case. The corresponding trajectory in axis-ratio space, shown in Figure 32, confirms that the void smoothly evolves toward sphericity even in the presence of dark energy.

11.4.1 Dark Energy as an Isotropic Amplifier

This set of results reveals a striking feature of void dynamics: the addition of dark energy does not disrupt the trend toward sphericity, it enhances it. While dark energy causes all axes to expand more rapidly, it does so in a manner that preserves their proportionality. This means that voids subjected to both self-gravity and cosmic acceleration grow not only faster, but also rounder.

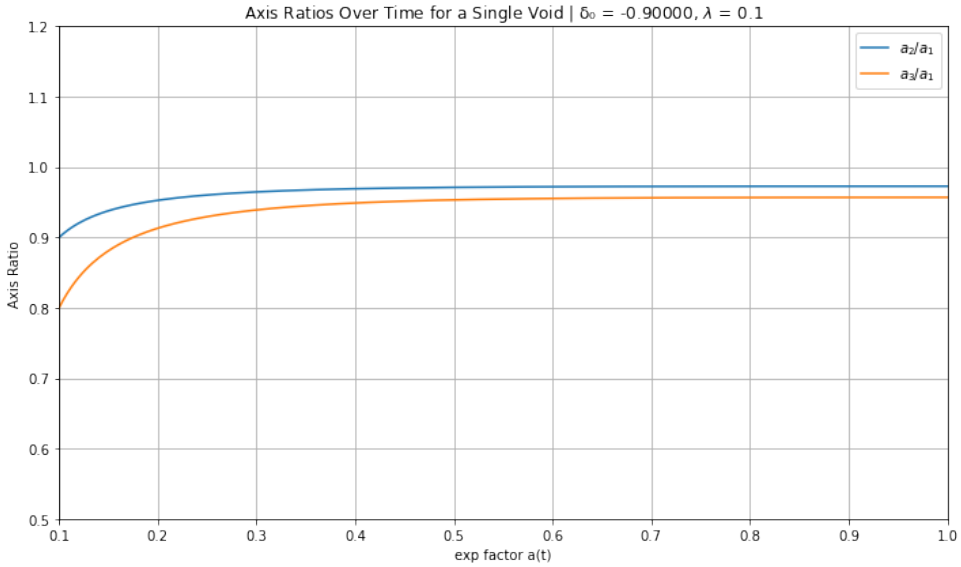

Figure 31: Axis ratio evolution for the same void. Both a_2/a_1 and a_3/a_1 increase steadily and asymptote near unity. This shows that the void's shape becomes increasingly spherical over time, even under the influence of a cosmological constant.

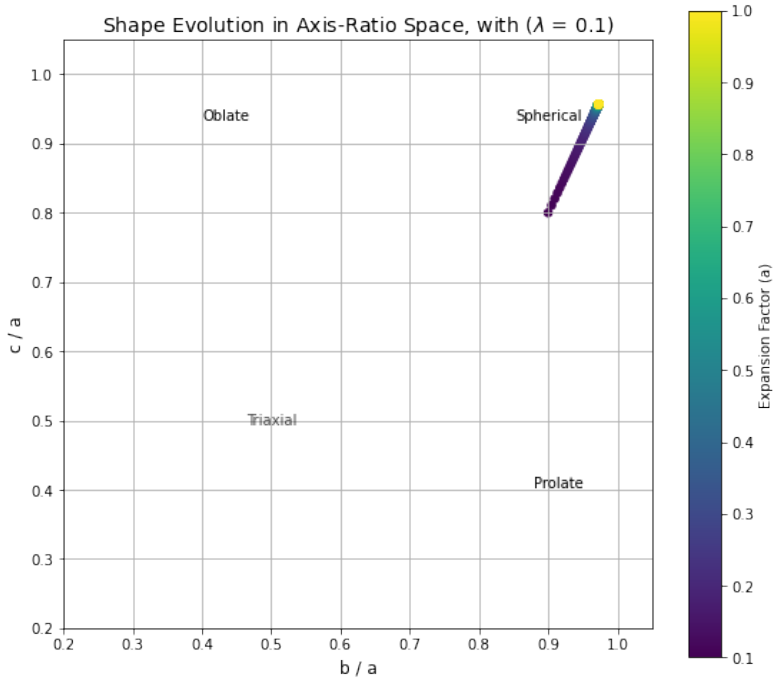

Figure 32: Trajectory in axis-ratio space for the evolving void with $\lambda = 0.1$. The system moves steadily toward the spherical point $(b/a, c/a) = (1, 1)$, confirming that dark energy does not hinder isotropization.

This behavior underscores a fundamental asymmetry in structure formation. Overdense regions become increasingly anisotropic during collapse, as gravitational forces act unevenly. In contrast, underdense regions, especially in a dark-energy-dominated era, evolve toward geometric simplicity. Voids do not collapse or fragment; they expand and smooth out.

In essence, dark energy acts as an isotropic amplifier. It inflates underdense regions while diluting both matter and geometric memory. The resulting voids retain the imprint of their initial triaxiality only faintly, drifting steadily toward spherical symmetry. This highlights a deep cosmological elegance: the large-scale emptiness of the universe becomes not just expansive, but orderly.

11.5 Impact of External Tidal Fields

To explore the effect of external shear, the same ellipsoidal underdensity with $\delta_0 = -0.9$ is evolved under a non-zero tidal field with eigenvalues $(-1, -1, 1)$. This configuration introduces directional anisotropy, enhancing expansion along the a_1 and a_2 axes and suppressing it along a_3. The background remains an Einstein–de Sitter universe ($\Omega_m = 1$, $\Lambda = 0$), and the initial axis ratios are $(a_1, a_2, a_3) = (1.0, 0.9, 0.8)$.

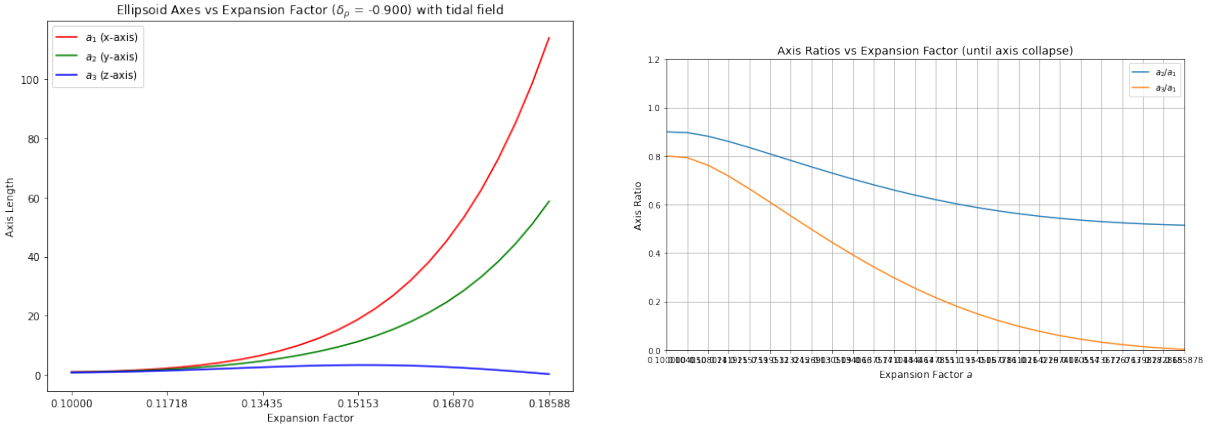

Figure 33: Left: Axis evolution for a void with $\delta_0 = -0.9$ under a tidal field with eigenvalues $(-1, -1, 1)$. The a_1 and a_2 axes expand rapidly, while a_3 slows, reverses, and collapses. Right: Axis ratios a_2/a_1 and a_3/a_1 as a function of scale factor. Anisotropy increases dramatically over time as the tidal field drives collapse along a_3.

The left panel of Figure 33 shows that a_1 and a_2 experience accelerated expansion, while a_3 halts and undergoes collapse. This leads to a flattening of the ellipsoid into a sheet-like geometry. The right panel quantifies the resulting deformation: the axis ratio a_3/a_1 drops rapidly to zero, indicating collapse, while a_2/a_1 decreases more gradually but still reflects growing anisotropy.

Unlike the self-gravity-only case, where voids evolve toward isotropy, the presence of an external tidal field promotes strong shape deformation. Instead of rounding out, the void becomes highly elongated along two axes and compressed along the third. This highlights how external shear can significantly alter void geometry and override the smoothing tendency seen in isolated evolution.

Shape Evolution in Axis-Ratio Space The impact of the tidal field is further illustrated in Figure 34, which shows the trajectory of the void in axis-ratio space. The color gradient traces the evolution with increasing scale factor.

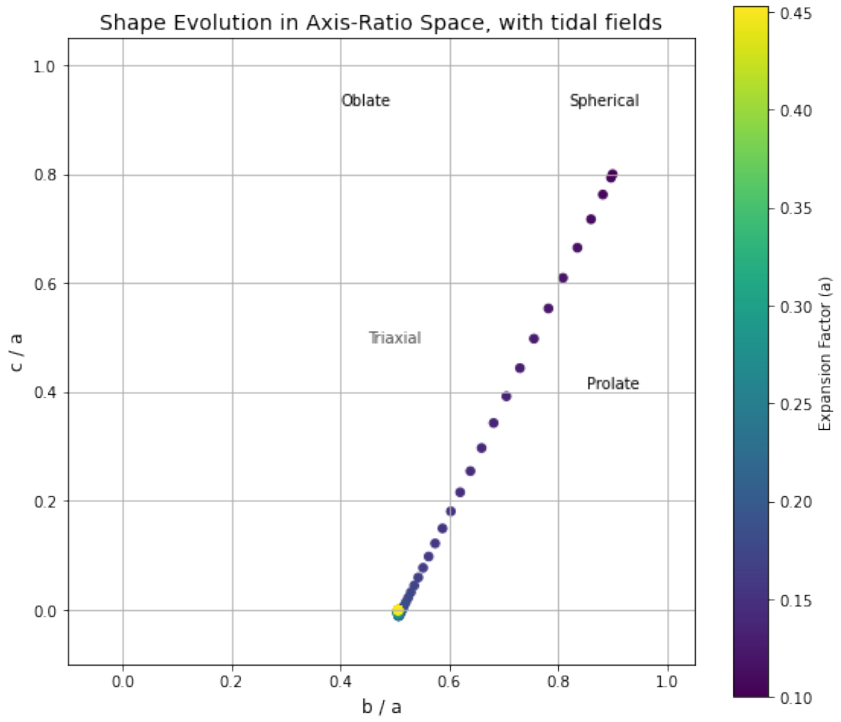

Figure 34: Trajectory of the void in axis-ratio space (b/a vs. c/a) under the influence of a tidal field. Color denotes the cosmological scale factor. The path moves rapidly toward the prolate regime as axis a_3 collapses and a_1 dominates.

Initially, the void occupies a mildly triaxial region. As evolution proceeds, the trajectory shifts sharply toward the prolate corner, reflecting the increasing elongation of the system. The collapse of axis a_3, combined with the accelerated growth of a_1, drives the void into a strongly anisotropic state. Unlike the self-gravitating case, where shapes symmetrize over time, the tidal field enforces a growing imbalance between axes, suppressing isotropization entirely.

This shape evolution underscores how external fields can dominate the morphological fate of voids, driving them into highly directional geometries even in the absence of collapse in all dimensions.

Visual Illustration of Anisotropic Evolution The dramatic impact of the tidal field on void morphology is clearly depicted in Figure 35. The plot shows the shape evolution of an ellipsoidal underdensity at three different expansion stages. As the universe expands from $a = 0.13$ to $a = 0.17$, the ellipsoid stretches significantly along the a_1 axis while the a_3 axis shrinks, reflecting collapse.

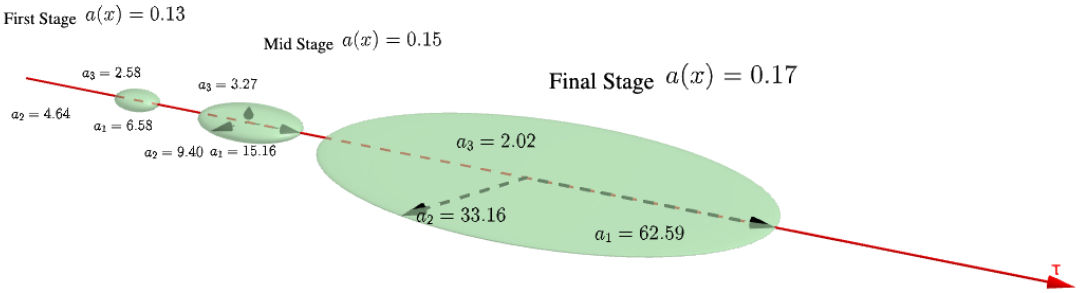

Figure 35: 3D visualization of the ellipsoid's evolution under a tidal field with eigenvalues $(-1, -1, +1)$. The snapshots show the deformation at three epochs, highlighting extreme stretching along the a_1 axis and contraction along a_3. The red arrow denotes the direction of the dominant tidal eigenmode.

This visualization reinforces the interpretation from axis and shape plots: the tidal field imposes strong directional growth and suppresses sphericalization. The system becomes increasingly elongated and anisotropic, with axis a_3 collapsing entirely while a_1 dominates the geometry. This behavior contrasts sharply with the symmetrizing trend observed in the self-gravity-only case.

12 TNG50 comparsion

I would like to begin this paragraph by expressing my sincere gratitude to Luuk Westerhoek, who generously provided the eigenvalue data from the TNG50 simulation, which made the second part of my analysis possible (Westerbroek, 2025).

12.1 Description of the Void Data

For the second part of this work I analyzed a void catalogue provided by (Westerbroek, 2025) consists of a sample of 100 randomly selected ellipsoidal underdensities from the TNG50 cosmological simulation. For each void, the three eigenvalues of the deformation tensor were extracted at three distinct cosmic epochs corresponding to redshifts $z = 20.05$, $z = 9.39$, and $z = 0.00$. From these eigenvalues, I computed the void axis lengths using the relation:

$$a_i = \frac{1}{\sqrt{\lambda_i}}, \quad i = 1, 2, 3.$$

This form allows us to follow the geometrical development of the voids through cosmic time.

When the entire sample was visually and statistically examined, it was clear that the voids display varied morphological behaviors. Some of the initially anisotropic voids have a tendency to move towards more spherical geometries, whereas others show growing anisotropy over time.

Considering the aim of this research simulating the evolution of voids that are roughly spherical initially and then become progressively more anisotropic, I used a selection criterion to pick the best representative examples. These chosen voids possess very large axis ratios (a_2/a_1 and a_3/a_1) at $z = 20.05$, and develop towards considerably smaller ratios by $z = 0.00$, showing an evident tendency to flatten or elongate. To demonstrate this evolution, I used plots of ratios of the axes a_2/a_1 vs. a_3/a_1 for the selected voids at each of the three redshifts. These plots clearly show the systematic deviation from sphericity and give qualitative grounds for using an ellipsoidal model of void dynamics (see Figures 36, 37, and 38).

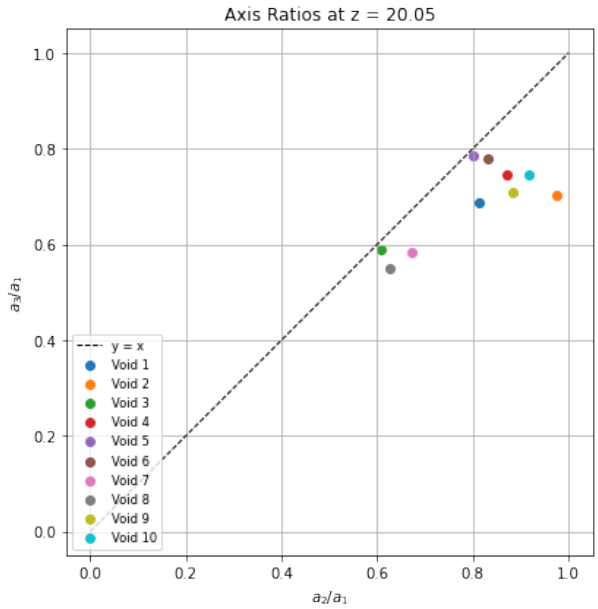

Figure 36: Axis ratio evolution for the 10 selected voids at redshift $z = 20.05$. Each point represents a void in the a_2/a_1 vs a_3/a_1 plane. Colors identify the same void across redshifts.

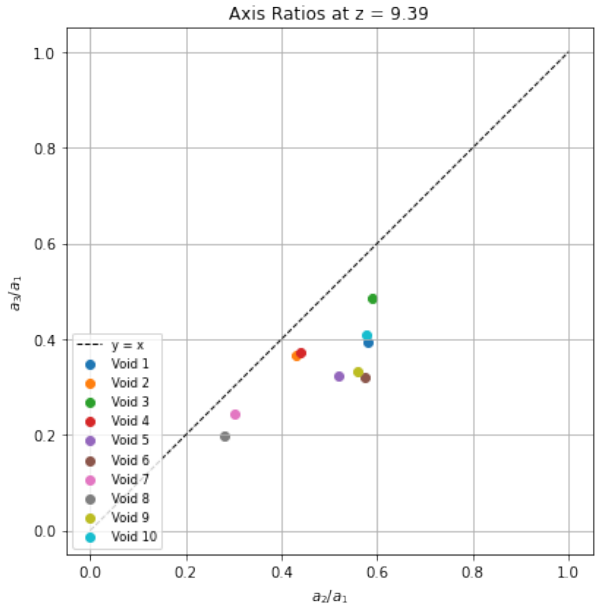

Figure 37: **Axis ratios at** $z = 9.39$ for the same set of voids

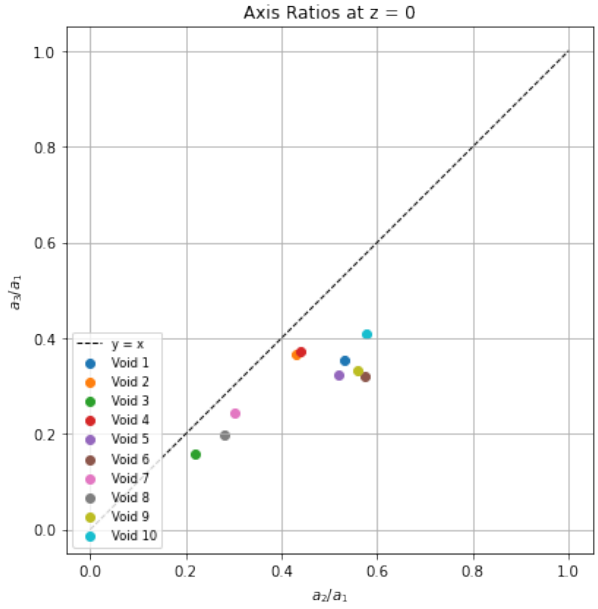

Figure 38: **Final axis ratios at redshift** $z = 0.00$

To complement the 2D analysis of axis ratios, I also produced 3D visualizations of the shape evolution for one representative void. These ellipsoids, shown in Figure 39, illustrate the change in physical scale and anisotropy over time. The void starts relatively compact and nearly spherical at high redshift and grows significantly in size while developing a more elongated geometry by the present day.

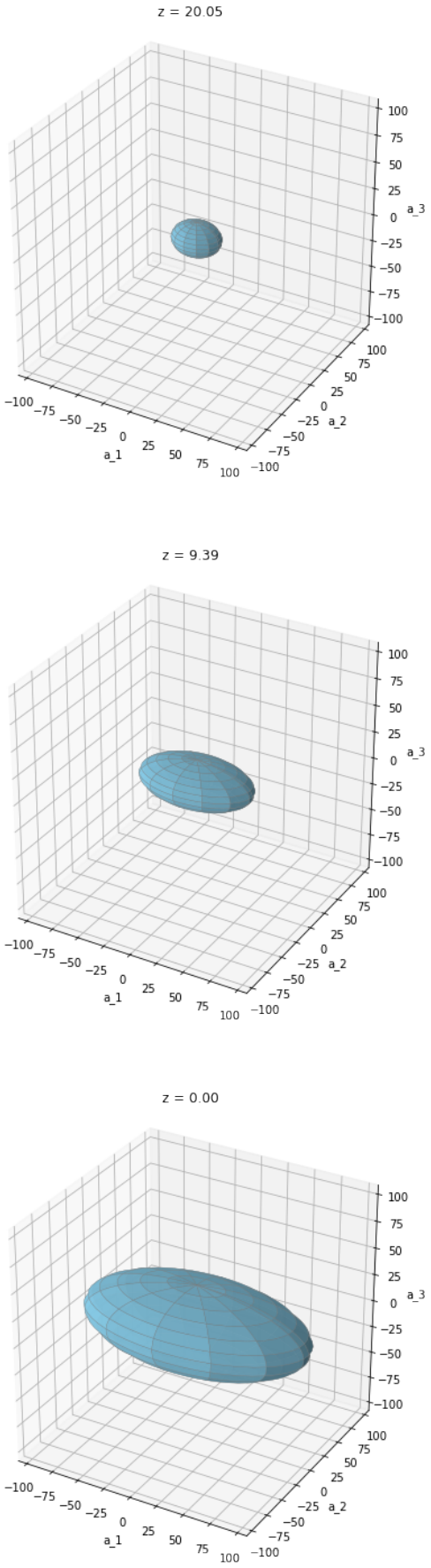

Figure 39: **3D visualization of a single void** evolving from high redshift ($z = 20.05$) to the present day ($z = 0.00$). The void expands in physical size and becomes more anisotropic with time, matching the trends seen in the axis ratio analysis.

12.2 Initial Conditions for the Simulation

The void evolution model developed in this thesis is initialized using physical parameters extracted from the TNG50 cosmological simulation at redshift $z = 20.05$, corresponding to an expansion factor of $a_i = 0.0475$. The following inputs were used:

- Normalized axis lengths $(a_1, a_2, a_3) = (1.000, 0.814, 0.688)$, computed from the eigenvalues of the initial density field provided by (Westerbroek, 2025). The axis lengths were obtained via:
$$a_i \propto \frac{1}{\sqrt{\lambda_i}},$$
where λ_i are the eigenvalues of the Hessian of the density field, and then normalized so that $a_1 = 1$. These characterize the initial shape of the proto-void.

- Initial underdensity $\delta_0 = -4.0086$, computed from the trace of the tidal tensor via:
$$\delta_0 = \lambda_1 + \lambda_2 + \lambda_3,$$
where $\lambda_1 = -1.9891$, $\lambda_2 = -1.4366$, and $\lambda_3 = -0.5829$ are the eigenvalues of the tidal field at the void center.

- Tidal field eigenvalues $\lambda_1 = -0.6$, $\lambda_2 = -0.1$, and $\lambda_3 = +0.7$ were used to define the anisotropic gravitational environment around the void. These eigenvalues were chosen to satisfy the traceless condition:
$$\lambda_1 + \lambda_2 + \lambda_3 = 0,$$
corresponding to the traceless part of the tidal tensor:
$$T_{ij}^{(\text{traceless})} = \frac{\partial^2 \phi}{\partial x_i \partial x_j} - \frac{1}{3}\delta_{ij}\nabla^2\phi.$$
This decomposition isolates the anisotropic effects from the isotropic density component, which is already accounted for by the initial underdensity δ_0.

13 Results of the Ellipsoidal Void Evolution Model

Using the ellipsoidal evolution model, we simulated the growth of a cosmic void embedded in a tidal environment characterized by the traceless eigenvalues $\lambda_1 = -0.6$, $\lambda_2 = -0.1$, and $\lambda_3 = +0.7$. The simulation was initialized at redshift $z = 20.05$ (scale factor $a = 0.0475$) using axis lengths derived from the TNG50 matter density field.

- **Initial axis lengths (at $z = 20.05$)**: $(a_1, a_2, a_3) = (1.000, 0.814, 0.688)$
- **Intermediate stage (at $z = 9.39$)**: $(a_1, a_2, a_3) = (3.449, 2.591, 1.825)$
- **Late stage (at $z = 5.50$)**: $(a_1, a_2, a_3) = (49.126, 15.488, 0.0154)$
- **Final stage (at $z = 0$)**: collapse

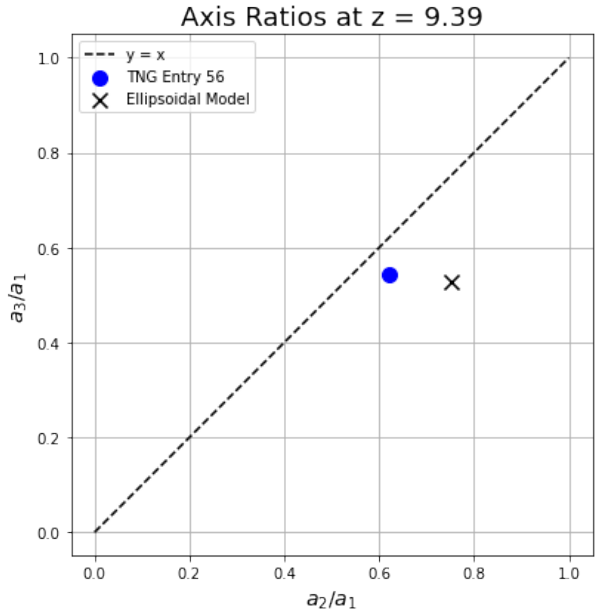

Figure 40: **Axis ratios from the model and TNG50 at** $z = 9.39$. The black cross represents the ellipsoidal model; the blue dot shows TNG50 data.

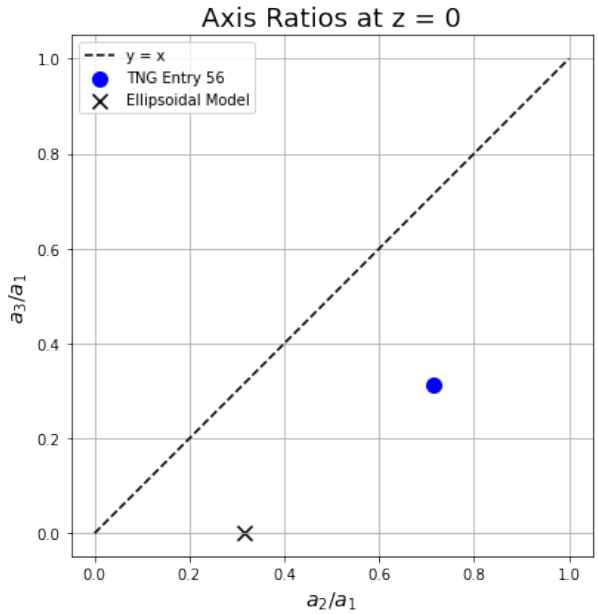

Figure 41: **Axis ratios from the model and TNG50** at $z = 0$. The black cross represents the ellipsoidal model just before the collapse, so redshift 5.5; the blue dot shows TNG50 data.

Analysis of Results and Comparison with TNG50

Due to time limitations, this research was able to test the ellipsoidal model on only a single void extracted from the TNG50 simulation. Although this lowers the statistical validity of the comparison, the selected void is still a useful initial test case to examine whether the model can capture the overall characteristics of void evolution in cosmological simulations. Generally, the

model reproduces the anticipated pattern for anisotropic growth: as it grows, the void stretches in shape and preferentially grows more along its larger axis a_1 than in its smaller axis a_3. This agrees with theoretical expectations of tidal influence from the ambient environment to grow more in underdense directions and less in overdense directions. At early times, and especially at $z \sim 20$, the model is in very good agreement with the TNG50 data for the axis ratios, which is reassuring.

At lower redshifts, however, the discrepancies arise. By $z \sim 5.5$, the model expects an extreme level of anisotropy, with the shortest axis all but collapsing. In the TNG50 void, on the other hand, there is continued expansion in all directions, and no collapse is witnessed even at $z = 0$. This then implies that the model might be overestimating the rate or extent of anisotropic growth, perhaps as a result of its oversimplifying assumptions.

A further point of interest is that, within the TNG50 data, the axis lengths at $z = 9.39$ were shorter than at $z = 20.05$. This is a little unexpected, since voids must grow monotonically in general. This evolution could be the result of local interactions, data extraction artefacts, or resolution effects, and adds uncertainty to the comparison.

We also observe that the test case was started at an extreme underdensity of $\delta = -4$, outside the normal range of model development ($\delta = -0.1$ to -0.9). Although helpful for testing the limits of the model, such a large initial contrast presumably enhances the anisotropy and hastens axis collapse, and so may be partially responsible for disagreement with the simulation at later times.

In spite of these problems, the fact that the model can qualitatively reproduce anisotropic expansion is a good result. A more quantitative study involving several voids and less severe initial conditions would be a natural continuation of this work.

14 Final Remarks

I am enthusiastic and satisfied with the results obtained during this thesis. The ellipsoidal model developed during this work was initially tested in the spherical limit and managed to reproduce the expected result for spherical underdensities. In addition, it was able to reproduce some of the most striking trends regarding the anisotropic evolution of cosmic voids, i.e., the growing elongation with time.

Most significantly, the allowed a close examination of the various contributions of the different forces acting in void growth.

One of the significant insights this study has revealed is that the dark energy term, taken out and applied by itself without any influences from the tidal field, results in purely isotropic expansion. The anisotropic effects on void evolution therefore appear to be dominated by the tidal field. This separation of contributions would have been difficult to investigate in full simulations, but the analytical model made this separation possible.

Compared to more realistic TNG50 simulation data, the model was able to mimic the general trend of anisotropic growth. However, with time limitations and only a single void being tested, there is still much to be accomplished in validating and perfecting the model further. In the future, I would prefer to push the model with even more severe initial underdensities and examine void evolution from even earlier redshifts. These follow-up investigations would test the model's limitations and calibrate its predictive capabilities, particularly when compared with simulation data over an even wider variety of environments.

Acknowledgments

I would like to deeply thank my supervisor, Rien van de Weijgaert, for guiding me through this project. His advice, patience, and encouraging approach to cosmology have been greatly valuable, and I am extremely grateful to have been able to work with him.

Special thanks also go to Luuk Westerhoek for allowing me permission to use his TNG simulation data. Without him, this thesis's comparison section, something which truly brought the project to the next level, would not have been possible.

I would also like to thank all members of my bachelor thesis research group for their consistent support, helpful feedback, and motivation throughout this process.

Most of all, I am most thankful to my friends and family for their support, encouragement, and patience during this journey.

I also thank OpenAI's ChatGPT, whose application assisted me in formatting tables, structuring sections, and fine-tuning the layout of this thesis within Overleaf. Its support allowed me to work more efficiently and focus on the scientific content.

References

Amanullah R., et al., 2010, The Astrophysical Journal, 716, 712

Bardeen J. M., Bond J. R., Kaiser N., Szalay A. S., 1986, Astrophysical Journal, 304, 15

Bertschinger E., 1985, The Astrophysical Journal Supplement Series, 58, 39

Blumenthal G. R., Faber S. M., Primack J. R., Rees M. J., 1984, Nature, 311, 517

Bond J. R., Myers S. T., 1996, The Astrophysical Journal Supplement Series, 103, 1–83

Bond J. R., Kofman L., Pogosyan D., 1996, Nature, 380, 603

Bos E. G. P., 2016, PhD thesis, University of Groningen, Kapteyn Astronomical Institute

Bos E., van de Weygaert R., Dolag K., Pettorino V., 2012, Monthly Notices of the Royal Astronomical Society, 426, 440

Boylan-Kolchin M., Springel V., White S., Jenkins A., Lemson G., 2009, Monthly Notices of the Royal Astronomical Society, 398, 1150

Cai Y.-C., Neyrinck M. C., 2025, Nature Astronomy, in press

Caldwell R. R., 2009, Physics Letters B, 545, 23

Cautun M., van de Weygaert R., Jones B. J. T., Frenk C. S., 2014, Monthly Notices of the Royal Astronomical Society, 441, 2923

Cautun M., Paillas E., Cai Y.-C., Bose S., Armijo J., Li B., Padilla N., Li Y., 2017, Monthly Notices of the Royal Astronomical Society, 468, 3368

Cautun M., Paillas E., Cai Y.-C., Bose S., Armijo J., Li B., Padilla N., 2018, Monthly Notices of the Royal Astronomical Society, 476, 3195

Chincarini G., Rood H. J., 1975, Nature, 257, 294–296

Colberg J. M., Pearce F., Foster C., et al., 2008, MNRAS, 387, 933–944

Colless M., et al., 2003, arXiv e-prints, pp astro–ph/0306581

Desjacques V., 2008, MNRAS, 388, 638

Doroshkevich A. G., 1970, Astrophysics, 6, 320

Dubinski J., da Costa L. N., Goldwirth D. S., Lecar M., Piran T., 1993, ApJ, 410, 458

Einasto J., Joeveer M., Saar E., 1980, MNRAS, 193, 353–375

Eisenstein D. J., Loeb A., 1995, The Astrophysical Journal, 439, 520

Feldbrugge J., Van De Weygaert R., 2023, Journal of Cosmology and Astroparticle Physics, 2023, 058

Fillmore J. A., Goldreich P., 1984, ApJ, 281, 1

Frieman J. A., Turner M. S., Huterer D., 2008, Annual Review of Astronomy and Astrophysics, 46, 385

Gregory S. A., Thompson L. A., 1978, The Astrophysical Journal, 222, 784

Gunn J. E., Gott J. R., 1972, ApJ, 176, 1

Guzzo L., et al., 2014, Astronomy & Astrophysics, 566, A108

Haider M., Steinhauser D., Vogelsberger M., Genel S., Springel V., Torrey P., Hernquist L., 2016, Monthly Notices of the Royal Astronomical Society, 457, 3024

Hamaus N., Sutter P. M., Wandelt B. D., 2014, Physical Review Letters, 112, 041304

Hamaus N., Sutter P., Lavaux G., Wandelt B. D., 2015, Journal of Cosmology and Astroparticle Physics, 2015, 036–036

Hicken M., et al., 2009, The Astrophysical Journal, 700, 1097

Huchra J. P., et al., 2012, The Astrophysical Journal Supplement Series, 199, 26

Icke V., 1984, Monthly Notices of the Royal Astronomical Society, 206, 1P

IllustrisTNG Collaboration 2024, The Next Generation Illustris (TNG) Project, https://www.tng-project.org

Kirshner R. P., Oemler A., Schechter P. L., Shectman S. A., 1981, The Astrophysical Journal Letters, 248, L57

Kitaura F.-S., et al., 2012, Monthly Notices of the Royal Astronomical Society, 427, L35

Kowalski M., et al., 2008, The Astrophysical Journal, 686, 749

Lavaux G., Wandelt B. D., 2010, Mon. Not. Roy. Astron. Soc., 403, 1392

Leclercq F., 2015, PhD thesis, Université Paris-Sud

Lee J., Park C., 2009, The Astrophysical Journal, 696, L10

Li B., Zhao H., Koyama K., 2012, Mon. Not. Roy. Astron. Soc., 421, 3481

Libeskind N. I., et al., 2018, Monthly Notices of the Royal Astronomical Society, 473, 1195

Lin C. C., Mestel L., Shu F. H., 1965, The Astrophysical Journal, 142, 1431

Linder E. V., 2008, Reports on Progress in Physics, 71, 056901

Llinares C., Mota D. F., Winther H. A., 2014, Astron. Astrophys., 562, A78

Mortonson M. J., Weinberg D. H., White M., 2014, arXiv preprint arXiv:1401.0046

Nadathur S., Hotchkiss S., 2015, Monthly Notices of the Royal Astronomical Society, 454, 889

Nelson D., et al., 2019, Monthly Notices of the Royal Astronomical Society, 490, 3234

Neyrinck M. C., 2008, Monthly Notices of the Royal Astronomical Society, 386, 2101

Paillas E., Paz D., Sgró M. A., Padilla N., 2019, Monthly Notices of the Royal Astronomical Society, 490, 3359

Pakmor R., Springel V., 2013, Monthly Notices of the Royal Astronomical Society, 432, 176

Pakmor R., Bauer A., Springel V., 2011, Monthly Notices of the Royal Astronomical Society, 418, 1392

Peacock J. A., et al., 2001, Nature, 410, 169

Peebles P. J. E., 1980, The large-scale structure of the universe. https://ui.adsabs.harvard.edu/abs/1980lssu.book.....P

Perlmutter S. e. a., 1999, The Astrophysical Journal, 517, 565–586

Pillepich A., et al., 2018, Monthly Notices of the Royal Astronomical Society, 473, 4077

Pisani A., Sutter P. M., et al., 2019, Bulletin of the AAS, 51, 40

Planck Collaboration et al., 2016, , 594, A13

Planck Collaboration Aghanim N., Akrami Y., et al., 2020, Astronomy & Astrophysics, 641, A6

Platen E., 2009, Phd thesis, University of Groningen

Platen E., van de Weygaert R., Jones B. J. T., 2007, Monthly Notices of the Royal Astronomical Society, 380, 551

Platen E., van de Weygaert R., Jones B., 2008, Monthly Notices of the Royal Astronomical Society, 387, 128

Riess A. G. e. a., 1998, The Astronomical Journal, 116, 1009–1038

Rodriguez-Gomez V., et al., 2015, Monthly Notices of the Royal Astronomical Society, 449, 49

Ryden B., 2003, Introduction to cosmology. https://ui.adsabs.harvard.edu/abs/2003itc..book.....R

Ryden B. S., Melott A. L., 1996, The Astrophysical Journal, 470, 160

Sheth R. K., van de Weygaert R., 2004, Monthly Notices of the Royal Astronomical Society, 350, 517

Springel V., 2010, Monthly Notices of the Royal Astronomical Society, 401, 791

Springel V., White S. D. M., Tormen G., Kauffmann G., 2001, Monthly Notices of the Royal Astronomical Society, 328, 726

Springel V., et al., 2005, Nature, 435, 629

Springel V., Frenk C. S., White S. D. M., 2006, Nature, 440, 1137

Tegmark M., et al., 2004, The Astrophysical Journal, 606, 702

Weinberger R., et al., 2017, Monthly Notices of the Royal Astronomical Society, 465, 3291

Westerbroek L., 2025, Private communication

White S. D. M., 1979, Monthly Notices of the Royal Astronomical Society, 186, 145

York D. G., et al., 2000, The Astronomical Journal, 120, 1579

Zavala J., Frenk C. S., 2021, Universe, 7, 219

Zel'dovich Y. B., 1970, , 5, 84

de Lapparent V., Geller M. J., Huchra J. P., 1986, The Astrophysical Journal, 302, L1

van de Weygaert R., 2016a, in , Springer Lecture Notes in Physics: The Zeldovich Universe

van de Weygaert R., 2016b, in Lecture Notes in Physics. Springer, pp 77–138

van de Weygaert R., Platen E., 2011a, International Journal of Modern Physics: Conference Series, 1, 41

van de Weygaert R., Platen E., 2011b, in Proceedings of the 2nd International Conference on the Dynamics of the Universe. World Scientific, pp 41–66 (arXiv:0912.2997), doi:10.1142/S2010194511000092

van de Weygaert R., Schaap W., 2009, in , Vol. 665, Data Analysis in Cosmology. pp 291–413, doi:10.1007/978-3-540-44767-2_11, https://ui.adsabs.harvard.edu/abs/2009LNP...665..291V

van de Weygaert R., van Kampen E., 1993, Monthly Notices of the Royal Astronomical Society, 263, 481